8-2007

Pulse Shape Analysis Studies in Si(Li) Detector

Rama S. Katakam
University of Tennessee - Knoxville

To the Graduate Council:

I am submitting herewith a thesis written by Rama S. Katakam entitled "Pulse Shape Analysis Studies in Si(Li) Detector." I have examined the final electronic copy of this thesis for form and content and recommend that it be accepted in partial fulfillment of the requirements for the degree of Master of Science, with a major in Physics.

Robert Grzywacz, Major Professor

We have read this thesis and recommend its acceptance:

Carrol Bingham, Stuart Elston

Accepted for the Council:
Carolyn R. Hodges

Vice Provost and Dean of the Graduate School

(Original signatures are on file with official student records.)

To the Graduate council:

I am submitting herewith a thesis written by Rama S Katakam entitled "Pulse Shape Analysis Studies in Si(Li) Detector". I have examined the final electronic copy of this thesis for form and content and recommend that it be accepted in partial fulfillment of the requirements for the degree of Master of Science, with a major in Physics.

Robert Grzywacz
Major Professor

We have read this thesis
and recommend its acceptance:

Carrol Bingham

Stuart Elston

Accepted for the Council:

Carolyn R. Hodges
Vice Provost and the Dean
of the Graduate School.

(Original signatures are on file with official student records.)

Pulse Shape Analysis studies in Si(Li) Detector

A Thesis

Presented for the

Master of Science

Degree

The University of Tennessee, Knoxville

Rama S Katakam

August 2007

Dedication

To my parents Sri. Veerabhadra Rao Katakam and Smt. Sarojini Katakam for their caring and endless love towards me. I love you.

Acknowledgements

I wish to thank all those who helped me complete my Master of Science degree in Physics. Special thanks to my advisor Dr. Robert Grzywacz for his guidance and encouragement through out this process. He was very supportive and patient in explaining things to me. He would always take time out of his busy schedule to answer my questions and check on my progress. Thank you Robert.

I would also like to thank my other committee members Dr. Carrol Bingham and Dr. Stuart Elston for their valuable suggestions and help on my thesis. Special thanks to Dr. Chiara Mazzocchi and Dr. Kate Jones Grzywacz for their help when I first started at UT. Many thanks to other group members of UT/HRIBF Nuclear Structure group. The informal scientific discussions over lunch were of great help to me.

Finally, I am forever indebted to my parents Veerabhadra Rao Katakam and Sarojini Katakam for their caring, endless love and encouragement. Without my parents I would have never come to the US and attend UT. Special thanks to my Sister and Brother-in-law for their support and love. I love you all. I thank my rocking friends at UT for their help and support.

Abstract

This work presents developments in the nuclear radiation detection, which take advantage of fast digital electronics. Numerical algorithms, which analyze detector pulse shape, were tested. A method to discriminate between electrons and gamma radiation using pulse shape analysis was demonstrated. The analysis was done on the data taken with ^{207}Bi source using a semiconductor Si(Li) detector. An algorithm to improve the timing resolution of the detection system was implemented. Software code to simulate the pulse shape generation process, for electrons and gamma radiation, in a Si(Li) detector was developed. Advantages of the applications of digital electronics in nuclear spectroscopy are discussed.

Contents

List of Figures

Chapter 1

Introduction

In modern day nuclear spectroscopy, data acquisition systems based on digital electronics are finding increasing use. The main characteristic differentiating these systems from so called "analog" systems is that the detector signals are converted into the digital form at the very early stage and the information about the detector pulse is extracted using purely numerical algorithms. The popularity of this approach can be attributed to its ability to store more complete information of the pulse and its inherent flexibility. The system can be adjusted or upgraded for specific application by the changes in the code without modifying the hardware. The most important demands of nuclear spectroscopy, low electronic threshold, energy resolution and good timing resolution are satisfied by digital electronics. This work tries to present such advantages of digital electronics in nuclear spectroscopy. The timing and pulse shape analysis algorithms for radiation detector data are implemented.

Studying nuclei far from stability requires great precision and detection efficiency in measurements. One important aspect of these measurements is the good timing resolution that can be achieved. In this work the abilities of fast digital electronics are used to develop a timing algorithm that can achieve a resolution as good as 3 ns, a fraction of the 25 ns sampling period (40MHz frequency) of the system. The timing algorithm is implemented and tested with the pulses produced by an electronic pulse

generator. This algorithm is then tested with the data taken using a semiconductor detector and a ^{207}Bi conversion electron source.

Revival of pulse shape discrimination (PSD) techniques has been enabled by proliferation of digital electronics. The gamma ray tracking and particle identification techniques are the most common applications [Vet00, Vet01, Del99, Amm63, Pau94, Mut99]. In this work we demonstrate the ability of the PSD technique to improve detection sensitivity of the semiconductor detector. We have developed a γ-ray background elimination technique for the conversion electron detector, which uses an algorithm differentiating between γs and electrons. Using a schematic model of interaction of radiation with matter, pulse shapes are simulated for electrons and γ rays interacting with the detector. These pulse shapes are analyzed to develop an algorithm for discriminating between electrons and γ rays for the data taken using a detector and ^{207}Bi source.

This document is organized as follows. First, the principles of interaction of electrons and γ rays with matter are discussed. Second, semiconductor devices as radiation detectors are discussed. Third, the potential and applications of digital electronics in nuclear spectroscopy are discussed. Then, the algorithms for timing resolution, pulse shape simulations and pulse shape analysis are presented and discussed. Finally, the results of this work and its applications are presented.

Chapter 2

Interaction of electrons and gamma radiation with matter

In experimental nuclear or particle physics, the knowledge of how radiation and particles interact with matter is of utmost importance. The knowledge of these interaction mechanisms greatly affects the design of the nuclear radiation detection schemes and experiments. The interaction mechanisms determine the sensitivity and efficiency of the detectors. The following is based on the discussion in [Leo94, Kno99].

In this chapter the interaction mechanisms of fast electrons and gamma radiation with matter are discussed. Table 2.1 shows different radiation types and sources.

Table 2.1: Types and sources of radiation.

Types of radiation	Specific examples	Sources of radiation
Charged particulate radiation	Fast electrons	Beta particles from nuclear decay, energetic electrons from other processes
	Heavy charged particles	Alpha particles and protons, Fission products and products of many nuclear reactions
Uncharged particulate radiation	Electromagnetic radiation	X-rays (Rearrangement of electron shells of atom), γ-rays (Transitions within the nucleus)
	Neutrons	Nuclear reactions

2.1 Sources of fast electrons

β decay

β decay is a decay process where a radionuclide decays by the emission of an electron or positron

$$ {}^{A}_{Z}X \rightarrow {}^{A}_{Z+1}Y + \beta^{-} + \overline{\nu} . $$

Here β^{-} is an electron and $\overline{\nu}$ is an antineutrino. Neutrinos and antineutrinos have very small interaction probability. The neutrino and the recoil nucleus Y have very small recoil energy. Therefore the only easily detectable radiation produced by β decay is a β particle (electron in case of β^{-} decay and positron in case of β^{+} decay).

Most β decays populate an excited state of the product nucleus and the subsequent de-excitation to a lower excited state occurs by the emission of γ rays. Therefore in most common β sources γ rays follow β particles. Nuclides that directly decay to the ground state of the product nucleus are called "pure β emitters". Ex: ^{3}H, ^{14}C etc.

Internal conversion

The nuclear process of internal conversion (IC) can be the source of conversion electrons, which are nearly monoenergetic. This process starts with an excited nuclear state, which may be formed by a preceding process (Ex: β decay to an excited state or nuclear reaction). Usually this excited state decays to the ground state or to a lower state by γ ray emission. But in some cases γ ray emission is inhibited (for example, due to high multipolarity of the transition) and the alternative is the process of internal conversion.

In this process the energy of the excited state, E_{exc}, is transferred directly to one of the orbital electrons of the atom. The energy of this electron then is given by

$$ E_{e^-} = E_{exc} - E_b . \qquad (2.1) $$

Here E_b is the binding energy of the electron in its original electron shell.

Since the conversion electron can come from many available electron orbits, the spectrum generally has many energy groups (discrete spectrum).

Ex: $^{207}_{83}Bi \rightarrow (EC) \rightarrow {}^{207}_{82}Pb^{*} \rightarrow (IC) \rightarrow {}^{207}_{82}Pb$ [App61] has conversion electron transitions with energies 481 keV, 553 keV, 975 keV and 1047 keV. The 481 keV and 553 keV are transitions between the level at 569 keV and the ground state of ^{207}Pb and correspond to de-excitation of the 569.7 keV line, which also decays via emission of 569.7 keV gamma ray. The 975 and 1047 keV are transitions between excited states at 1633.4 keV and 569.7 keV, also de-exciting via gamma ray transition of 1063.7 keV, see figure 2.1. These electron and gamma transitions are part of a de-excitation cascade from the level at 1633.4 keV populated in the beta decay of ^{207}Bi. This coincidence is exploited in the measurement to measure the timing resolution achievable with the timing algorithm, explained later in chapter 6.

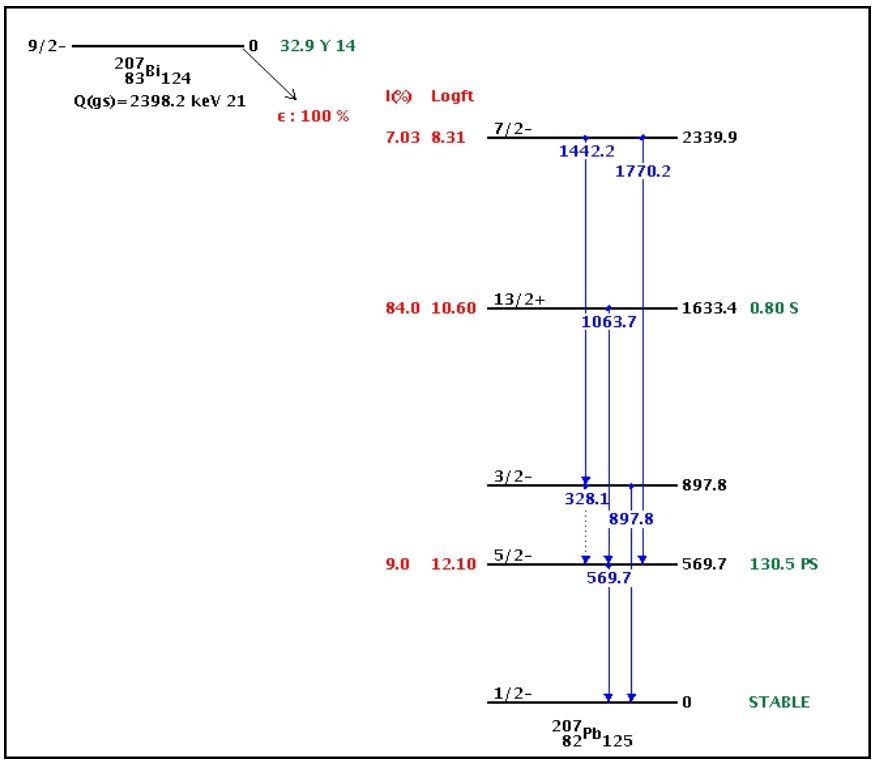

Figure 2.1: Decay scheme of 207Bi [NNDC]. Arrows indicate transitions between levels associated with emission of gamma rays.

Auger electrons

Auger electrons are analogues of conversion electrons. The excitation energy originates in the atom rather than in the nucleus. A preceding process, such as electron capture, which is the process where a nucleus captures an electron from an inner atomic shell, may leave an atom with a vacancy in one of it's normally filled electron shells. Usually an electron in one of the outer shell fills this vacancy and emits a characteristic X-ray. Alternatively, this excitation energy is transferred directly to one of the outer electrons and this electron gets ejected. This electron is called an Auger electron. Its energy is given by

$$E_{e^-} = E_{exc} - E_b \,, \tag{2.2}$$

where E_b is the binding energy of the electron in its original electron shell.

The spectrum is discrete as in the case of Internal conversion. The energy of Auger electrons is relatively low compared to β particles or conversion electrons, typically a few keV. This process is favored only in low Z elements. Auger electrons can be easily stopped in thin source covers or detector entrance windows.

2.2 Sources of gamma radiation

Gamma rays following β decay

Gamma radiation is emitted by an excited nucleus in its transition to a lower nuclear level. This excited nucleus may be, for example, created in the decay of a radionuclide. The γ-ray energy is equal to the difference in energy between the initial and final states. The γ-rays appear with a half-life characteristic of the parent nucleus and the energy reflects the energy level structure of the daughter nucleus. Because nuclear states have well defined energies, the energies of the γ-rays are specific and are nearly monoenergetic.

Annihilation radiation

An additional electromagnetic radiation is generated during the β^+ decay. This is because of the positrons emitted in the decay process. Since positrons travel only few millimeters before losing their kinetic energy, they are usually absorbed in the

encapsulation around the source. Near the end of their range, they combine with the electrons in the absorbing material. This process is called annihilation. The electron-positron pair disappears and is replaced by two oppositely directed 511 keV electromagnetic photons called annihilation radiation.

Gamma rays following nuclear reactions

Processes such as nuclear reactions can lead to the population of higher-lying nuclear states, which can emit high-energy γ-rays, whose energy is higher than the γ-rays from β active radioisotopes. Examples of such reactions can be

$$^{4}_{2}\alpha + {}^{9}_{4}Be \rightarrow {}^{12}_{6}C + {}^{1}_{0}n$$

In this reaction the product nucleus ^{12}C is left in an excited state. Its decay can give rise to γ-rays of 4.44MeV energy.

$$^{4}_{2}\alpha + {}^{13}_{6}C \rightarrow {}^{16}_{8}O + {}^{1}_{0}n$$

In this reaction the product nucleus ^{16}O is left in an excited state. Its decay can give rise to γ-rays of 6.13MeV energy.

Gamma rays are also emitted following the absorption of thermal neutrons. These "neutron-capture gamma rays" typically have energies ranging as high as 9 MeV.

Bremsstrahlung

When fast electrons interact with matter, part of their energy is converted into electromagnetic radiation in the form of bremsstrahlung. This fraction increases with electron energy and atomic number of the absorbing material. This type of radiation can also be produced by other sources of fast electrons including beta particles. In addition to bremsstrahlung, characteristic X-rays are also produced when fast electrons interact with matter. Therefore the spectra for bremsstrahlung sources also show characteristic X-ray lines superimposed on the continuous bremsstrahlung spectrum.

2.3 Interaction of electrons with matter

When interacting with matter, electrons lose their energy by Coulomb interaction with the electrons and the nuclei of the absorbing material. The collision of electrons with free and bound electrons results in the ionization or excitation of the absorbing

atom. Because of the very light mass of the electrons, collision with nuclei of the absorbing material leads to the intense scattering of electrons. Large deviations in the trajectory of the electrons in the material are possible since the mass of the electrons is much smaller than the nuclear mass. The trajectory is a jagged line. In addition to the inelastic collisions, radiative processes such as bremsstrahlung can be dominating when electrons with energies more than few MeV interact with matter.

Energy loss

An expression has been derived by Bethe to describe the energy loss due to ionization and excitation for fast electrons given by

$$-\left(\frac{dE}{dx}\right)_c = \frac{2\pi e^4 NZ}{m_0 v^2}\left(\ln\left(\frac{m_0 v^2 E}{2I^2\left(1-\beta^2\right)}\right) - \ln 2\left(2\sqrt{1-\beta^2}-1+\beta^2\right)+\left(1-\beta^2\right)+\frac{1}{8}\left(1-\sqrt{1-\beta^2}\right)^2\right) \quad (2.3)$$

Here $\beta \equiv v/c$, N and Z are number density and atomic number of the absorber atoms, v is the velocity of the primary particle and m_0 and e are the rest mass and charge of the electron. The deflection of an electron in its interaction with absorber corresponds to an accelerating charge, which, according to classical theory, radiates its energy.

The linear specific energy loss through this radiative process is

$$-\left(\frac{dE}{dx}\right)_r = \frac{NEZ\left(Z+1\right)e^4}{137 m_0^2 c^4}\left(4\ln\frac{2E}{m_0 c^2}-\frac{4}{3}\right). \quad (2.4)$$

The total linear stopping power for electrons is the sum of collisional and radiative losses

$$\frac{dE}{dx} = \left(\frac{dE}{dx}\right)_c + \left(\frac{dE}{dx}\right)_r. \quad (2.5)$$

For electrons of interest (such as β particles or secondary electrons from γ-rays), typical energies are less than few MeV. The radiative losses are always a very small fraction of the energy losses due to ionization and excitation.

Absorption

The concept of range is less definite for fast electrons interacting with matter. Rather, the concept of zero-transmission range is introduced. This is done by means of absorption measurements. An absorbing material is placed between the source of fast

electrons and a detector. Because of the scattering of electrons from the absorbing material, even small values of absorber thickness leads to significant loss of electrons striking the detector. A plot of detected electrons and thickness, called transmission plot, would begin to drop and gradually approaches zero for large thicknesses, figure 2.15 in [Kno99]. The zero-transmission range is found from the transmission plot by extrapolating the linear portion of the curve to zero. The energy loss of electrons is much lower than that of heavy charged particles, so their path lengths, in typical materials, are typically hundreds of times greater.

The transmission curve for β particles differs significantly, because of their continuous distribution of energies, from that for fast electrons. The low-energy β particles are rapidly absorbed even in small thicknesses of the absorber. This results in a much greater slope on the transmission curve at small thicknesses. The rest of the curve has an exponential shape.

$$\frac{I}{I_0} = e^{-nt}. \tag{2.6}$$

Here I_0 is the counting rate without absorber, I is the counting rate with absorber, n is the absorption coefficient and t is the absorber thickness in g/cm^2.

Backscattering

The phenomenon of backscattering originates from the fact that electrons often undergo large deflections. Sometimes an electron might undergo sufficient deflection that it can re-emerge from the surface through which it entered. These backscattered electrons do not deposit all of their energy in the detector and can have significant effect on the response of the detector. Electrons backscattering from the top layer or entrance window of the detector will escape detection entirely. Backscattering is dominant for low-energy electrons and for high Z absorbing materials.

2.4 Interaction of γ-rays with matter

Three major types of interaction mechanisms play important roles in γ radiation measurements. They are the photoelectric absorption, Compton scattering and pair production. All these processes result in partial or complete transfer of the γ-ray energy

to electron energy. The γ-ray photon either disappears entirely or scatters through a large angle. This is in contrast to charged particles, which slow down gradually through continuous and simultaneous interactions with many absorber atoms. The concepts of specific ionization loss and ranges cannot be applied here. The corpuscular description of electromagnetic radiation is the most appropriate for these interaction mechanisms. One photon disappears at each interaction. Therefore the attenuation of photon beam can be described by

$$N = N_0 \exp(-\mu x) \tag{2.7}$$

Here N_0 is the original number of photons in the beam, N is the remaining photons after traversing distance x and μ is the absorption coefficient, which is the sum of three terms due to all the above processes.

Photoelectric absorption

In this process, a γ-ray photon interacts with an absorber atom and then completely disappears. An energetic photoelectron is ejected by the atom from one of its bound shells in its place. This interaction cannot take place with a free electron and takes place with the atom as a whole. The most probable origin of this photoelectron is the tightly bound K shell. The energy of this photoelectron would be

$$E_{e^-} = h\nu - E_b, \tag{2.8}$$

where E_b is the binding energy of this photoelectron in its original shell. For γ-rays with more than few hundred keV, the photoelectron carries off most of the original photon energy.

This process creates an ionized atom with a vacancy in one of its shells. This is filled through capturing of a free electron from the medium and/or rearrangement of electrons from other shells of the atom. This results in generating one or more characteristic x-ray photons. In most cases these x-ray photons are reabsorbed through photoelectric absorption and they can also escape. In some cases an Auger electron might be ejected in place of the characteristic x-ray to carry off the atomic excitation energy. This process is predominant for γ-rays with low energy. The probability for the photoelectric interaction is

$$\tau \approx const * \frac{Z^n}{E_\gamma^{3.5}}, \tag{2.9}$$

where the exponent n varies between 4 and 5. Therefore materials with high Z are usually chosen for γ-ray detection medium.

Compton scattering

This interaction takes place between the incident γ-ray and an electron in the absorbing material. This interaction is predominant for medium energy γ-rays (γ-rays from typical radioisotope sources). The γ-ray photon is deflected by θ and transfers a portion of its energy to the electron, which is then called recoil electron. The energy transferred may range from zero to a large fraction of the γ-ray energy depending upon the scattering angle.

Using conversation of energy and momentum, we can show that

$$h\nu' = \frac{h\nu}{1+\frac{h\nu}{m_0c^2}(1-\cos\theta)}. \tag{2.10}$$

Here m_0c^2 is the rest mass energy of the electron (0.511 MeV), $h\nu$ and $h\nu'$ are energies of the incident and scattered photons. Even in the extreme case of θ=π some energy is always retained by the incident γ-ray. The probability for Compton scattering per atom of the absorber depends on the number of electrons available as scattering targets, therefore increases linearly with Z.

The differential scattering cross section, $\frac{d\sigma}{d\Omega}$, is given by

$$\frac{d\sigma}{d\Omega} = Zr^2\left(\frac{1}{1+\alpha(1-\cos\theta)}\right)^2\left(\frac{1+\cos^2\theta}{2}\right)\left(1+\frac{\alpha^2(1-\cos\theta)^2}{(1+\cos^2\theta)\left[1+\alpha(1-\cos\theta)\right]}\right), \tag{2.11}$$

Where $\alpha \equiv h\nu / m_0c^2$ and r is the classical electron radius.

Pair Production

This interaction is energetically possible if the γ-ray energy exceeds twice the rest mass energy of an electron (~ 1.02 MeV). The probability for this interaction remains low

until the γ-ray energy reaches few MeV. This process is predominant for high-energy γ-rays.

This interaction takes place in the coulomb field of the nucleus. The γ-ray photon disappears and is replaced by an electron-positron pair. All the energy above 1.02 MeV carried by the γ-ray goes into the kinetic energy shared by the electron-positron pair. The positron annihilates after slowing down in the medium, creating two annihilation photons. The probability is approximately proportional to Z^2.

Chapter 3

Semiconductor Detectors

The following is based on the discussion in [Leo94, Kno99].

In the detection of radiation, use of solid-state detectors provides several advantages. Because material densities are about 1000 times greater than that of gas, detectors can be made much smaller than gas filled detectors, because of greater interaction probabilities. Semiconductor detectors are widely used in the detection of high-energy electrons and γ-rays. These detectors are based on crystalline semiconductor materials, like silicon or germanium. For charged particle detection and γ-ray spectroscopy, semiconductor detectors achieve better energy resolution than is possible with any other detector type.

The basic principle of operation is similar to that of a gas filled detector. The incident radiation creates electron-hole pairs along its path, which are collected using an applied electric field. The advantages of semiconductors can be put as follows. The energy required to create an electron-hole pair is very small, thus creating a large number of charge carriers. Semiconductors have greater stopping power, because of greater density. They are compact in size and have good timing characteristics. The effective thickness of the detector can be varied to match the experimental requirements. However, semiconductor detectors are highly sensitive to radiation damage, which may quickly degrade their performance. An additional cryogenic system may be needed to cool semiconductor material to low temperatures before they can be operated.

In this chapter different types of semiconductor detectors, their characteristics and operation are discussed starting with a brief review of basic semiconductor physics.

3.1 Semiconductor properties

Energy band structure

In crystalline materials, outer electronic shells exhibit an energy band structure. The structure consists of a valance band, a forbidden energy gap and a conduction band. There are many discrete energy levels closely spaced in the energy bands. A forbidden energy gap is a region where there are no energy levels available. These band structures arise from the periodic arrangement of the atoms in the crystals, which causes overlapping of the electron wave functions.

Electrons in the conduction band are detached from the parent atom and are free to roam around the crystal. Electrons in the valance band are more tightly bound. The widths of the gap and bands are determined by the lattice spacing of the atom. Therefore these parameters depend on temperature and pressure. In insulators the forbidden gap is large, in conductors it is non-existent and in semiconductors it is intermediate in size, as shown schematically in figure 3.1. In a semiconductor, a few electrons get excited into the conduction band from the valance band by thermal excitation. Therefore when an electric field is applied a small electric current is observed.

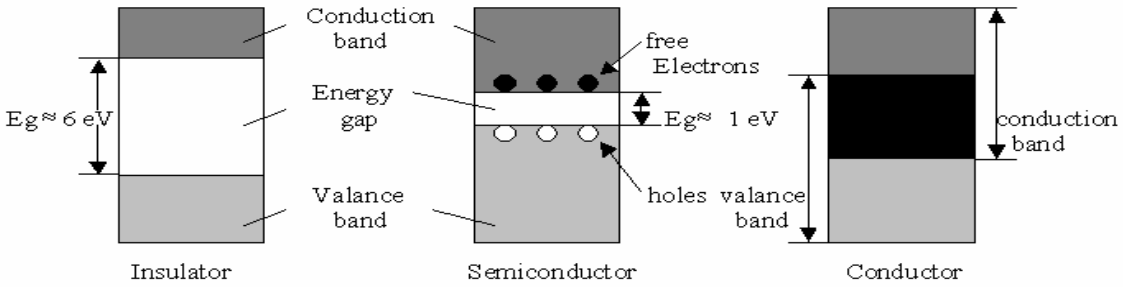

Figure 3.1: Energy band structure of conductors, insulators and semiconductors.

Charge carriers

At 0K, in the lowest energy state of the semiconductor, all the electrons in the valance band participate in the covalent bonding between the lattice atoms. However, at room temperatures, thermal energy can excite an electron across the energy gap into the conduction band. This leaves a vacancy, a "hole", in the valance band and is quickly filled by the neighboring electron, leaving another hole in its place to be filled by another neighboring electron. If this sequence goes on, the hole appears to move through the crystal. Since a hole is positive in charge, it acts like a positive charge carrier and its movement also contributes to the electric current. Therefore in semiconductors electric current arises from the movement of electrons in the conduction band and holes in the valance band.

In semiconductors, thermal energy constantly generates electron-hole pairs. At the same time a few electrons and holes recombine. Under stable conditions, an equilibrium concentration of electron-hole pair is established.

$$n_i = \sqrt{N_c N_v}\exp\left(\frac{-E_g}{2KT}\right) = AT^{3/2}\exp\left(\frac{-E_g}{2KT}\right) \tag{3.1}$$

Here n_i is the concentration of electrons (or equally holes), T is the temperature, N_c is the number of states in conduction band, N_v is the number of states in valance band, E_g is the energy gap at 0K and K is the Boltzmann constant. Both N_c and N_v can be derived from the Fermi-Dirac distribution and they both vary as $T^{3/2}$. A on the right hand side of the equation 3.1 is a constant. For Si, at 300K, typical n_i are on the order of $1.5\text{x}10^{10}$ cm^{-3}.

Mobility

When an external electric field is applied to a semiconductor, electrons and holes drift inside the semiconductor: electrons towards the positive side and holes towards negative side. The velocity with which they drift can be written as

$$\begin{aligned} v_e &= \mu_e E \\ v_h &= \mu_h E \end{aligned} \tag{3.2}$$

Here E is the magnitude of the applied electric field and μ_e ($\approx 3.1\text{x}10^4$ $cm^2/V.s$) and μ_h ($\approx 1.1\text{x}10^4$ $cm^2/V.s$) are the mobilities of the electrons and holes respectively. The mobilities

are functions of E and the temperature T, for a given material. The mobilities determine the current in a semiconductor. The current density is $J = \rho v$, where ρ is the charge density and v is the drift velocity. In a pure semiconductor J is given by

$$J = en_i(\mu_e + \mu_h)E \tag{3.3}$$

where n_i is the concentration of electrons (or equally holes). The equation contains the fact both electrons and holes are charge carriers in a semiconductor. The conductivity, which is the inverse of resistivity, $\sigma = J / E$ is then given by

$$\sigma = en_i(\mu_e + \mu_h)\,. \tag{3.4}$$

Recombination and Trapping

Recombination is a process, which is the exact opposite of electron-hole generation, in which an electron in the conduction band drops into an open level in the valance band, emitting a photon. However, the fact that electrons and holes have lifetimes as long as a second shows that the process of recombination is not the only process involved.

The impurities present in the crystal perturb the energy band structure and create additional energy levels in the middle of the forbidden gap. These levels can capture an electron from the conduction band and hold it for a certain holding time and then release it back into the conduction band. During the hold time it can also capture a hole, which then annihilates with the trapped electron. These energy levels are called the recombination centers. Each center can participate in many recombinations.

The existence of these recombination centers reduce, for radiation detection, the mean time charge carriers remain free for collection. If this time is less than the time it takes to collect the charges, charge loss will occur resulting in the reduction of resolution. Semiconductor detectors, therefore require relatively pure crystals.

Impurities in the crystal can also result in trapping. Some impurities are only capable of capturing one kind of charge carriers, electrons or holes, but not both. They will then hold the charge carriers for a certain holding time and release it back. If this holding time is of the order of charge collection time, charges will be lost. On the other hand if it is less than charge collection time little or no effect occurs. Structural defects

such as dislocations and vacancies in the lattice or atoms, which can arise from thermal shock and bombardment with radiation etc, can also cause energy levels in the forbidden gap.

3.2 Doped semiconductors

While impurities in the crystal lead to recombination and trapping effects, doping the semiconductor with certain impurities may also enhance the characteristics of the crystal. The difference between recombination and trapping impurities and these doping impurities is the position in the forbidden gap where the energy levels are created. Recombination and trapping impurities create deep levels near the middle of the forbidden gap, whereas doping impurities create shallow levels very close to conduction or valance bands.

Semiconductor doping

In a pure semiconductor crystal, also called intrinsic semiconductor, the number of holes equals the number of electrons in the valance band. These crystals can be doped with impurity atoms that have one more or one less valance electrons in their outer shells. They are called doped or extrinsic semiconductors.

If the dopant is pentavalent, one free electron is left and cannot be fit into the valance band. To accommodate this electron, an energy level is created in the energy gap. This level is very close to the conduction band, with separation of about 0.01eV for Ge and about 0.05eV for Si. An electron in this level can easily be excited into the conduction band, increasing the conductivity of the semiconductor. The extra electron increases the electron concentration and decreases the hole concentration. These semiconductors are called n-type semiconductors. Electrons are the majority charge carriers in n-type semiconductors with holes being the minority charge carriers. Commonly used impurities to make n-type materials, called donor elements, are arsenic, phosphorous and antimony.

If the dopant is trivalent, there will be an excess of holes in the crystal. This creates an energy level in the energy gap close to the valance band. Electrons in the valance band can easily be excited into this energy level, creating a hole in the valence

band. This excess of holes decreases the electron concentration. These semiconductors are called p-type semiconductors. Holes are the majority charge carries in p-type semiconductors with electrons being the minority charge carries. Commonly used impurities to make p-type materials, called acceptor elements, are lithium, gallium, boron and indium. Figure 3.2 [Leo94, Kno99] shows the creation of energy levels in energy gap with doping for n-type and p-type materials.

At thermal equilibrium, the positive and negative charge densities are equal, since a semiconductor is neutral. Therefore

$$N_D + p = N_A + n, \tag{3.5}$$

where N_D and N_A are the donor and acceptor concentrations. In an n-type material, the electron density is

$$n \approx N_D, \tag{3.6}$$

And the hole density is

$$p \approx \frac{n_i^2}{N_D}. \tag{3.7}$$

The conductivity of an n-type material is given by

$$\frac{1}{\rho} = \sigma = eN_D\mu_e. \tag{3.8}$$

An analogous result is found for the p-type materials.

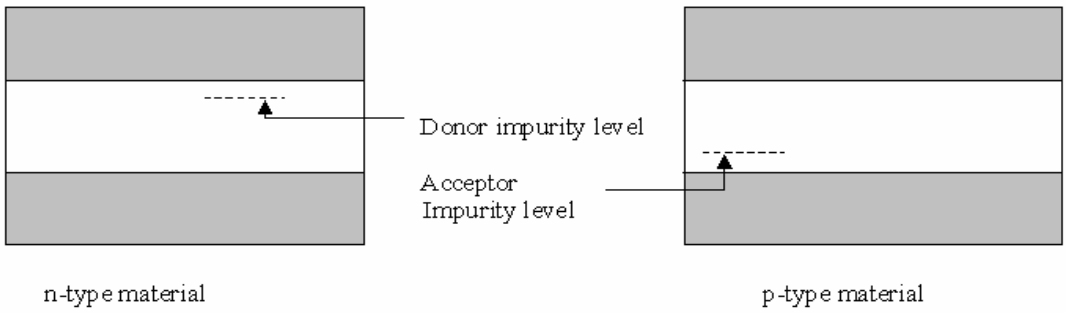

Figure 3.2: Creation of energy levels in energy gap with doping.

Semiconductor junction

The formation of a semiconductor junction determines the functionality of a semiconductor detector. One way to create this junction is to diffuse p-type impurities into one end of an n-type material. Because of the difference in concentrations of holes and electrons between the two materials, there will be an initial diffusion of electrons towards the p-region and holes towards n-region. The holes recombine with some electrons on the n-side and the electrons fill up some holes on the p-side. This diffusion makes the p-region electrically negative and the n-region positive, creating an electric field gradient across the junction. The creation of this electric field gradient eventually halts the diffusion. The potential difference across the junction is called the contact potential and the energy band structure of the semiconductor shifts by this potential.

The region with changing electric potential is called the depletion region. Any charge carrier, electron or hole, created or entering this region is swept away by this electric field gradient. This fulfills the basic functionality of a detector. Any ionizing radiation entering the semiconductor material liberates electron-hole pairs, which are then swept out by the electric field. A current signal proportional to the ionization can be detected if electrical contacts are placed on both ends of the junction device.

The width of this depletion region, called depletion depth, depends on the concentrations of n and p impurities and in general is small. The extent of the depletion region into the n-side, x_n, and into the p-side, x_p, are derived to be

$$x_n = \left(\frac{2\varepsilon V_0}{eN_D\left(1+N_D/N_A\right)} \right)^{1/2} \text{ and } x_p = \left(\frac{2\varepsilon V_0}{eN_A\left(1+N_A/N_D\right)} \right)^{1/2}. \tag{3.9}$$

The depletion depth, d, is then given by

$$d = x_n + x_p = \left(\frac{2\varepsilon V_0}{e} \frac{\left(N_A+N_D\right)}{N_A N_D} \right)^{1/2}. \tag{3.10}$$

Here V_0 and ε are contact potential and permitivity respectively. Here we can see that the depletion region extend farther into the lighter doped zone. Substituting typical values, for silicon

$d \approx 0.53(\rho_n V_0)^{1/2}\ \mu m$ for n-type, (3.11)

$d \approx 0.32(\rho_p V_0)^{1/2}\ \mu m$ for p-type. (3.12)

And for germanium

$d \approx (\rho_n V_0)^{1/2}\ \mu m$ for n-type, (3.13)

$d \approx 0.65(\rho_p V_0)^{1/2}\ \mu m$ for p-type. (3.14)

where ρ is the resistivity in Ωcm and V_0 is the contact potential in Volts.

The capacitance of the depletion region, because of its approximate planar geometry, can be approximated as

$$C = \varepsilon \frac{A}{d}. \quad (3.15)$$

where A is the area of the depletion region and d is its width and ε is the dielectric constant.

Approximately for silicon

$\frac{C}{A} = 2.2(\rho_n V_0)^{-1/2}\ pF/mm^2$ for n-type, (3.16)

$\frac{C}{A} = 3.7(\rho_p V_0)^{-1/2}\ pF/mm^2$ for p-type. (3.17)

And for germanium

$\frac{C}{A} = 1.37(\rho_n V_0)^{-1/2}\ pF/mm^2$ for n-type, (3.18)

$\frac{C}{A} = 2.12(\rho_p V_0)^{-1/2}\ pF/mm^2$ for p-type.. (3.19)

Reverse bias

The functionality of a pn junction semiconductor device as a detector can be enhanced using a reverse bias. The typical depletion region width of a pn junction is not sufficient to stop high-energy particles and cannot provide efficient charge collection. Better results can be achieved by applying a reverse bias voltage to the pn junction, i.e., a negative voltage to the p-side. This will result in attracting the holes in the p-region

away from the depletion region and similarly attracting the electrons in the n-side away from the depletion region, as illustrated in figure 3.3. This will enlarge the depletion region and thus makes the pn junction good enough for radiation detection.

The resistance of the semiconductor limits the maximum reverse bias voltage that can be applied. At some point, the junction breaks down and starts conducting. With current high resistivity silicon, depletion depths up to 5mm can be achieved. And even greater depths can be achieved by using high purity semiconductors.

3.3 Semiconductor as a detector

As discussed earlier reverse biased semiconductor pn junction devices provide good means of radiation detection. The basic configuration of a semiconductor diode as detector is shown in figure 3.4.

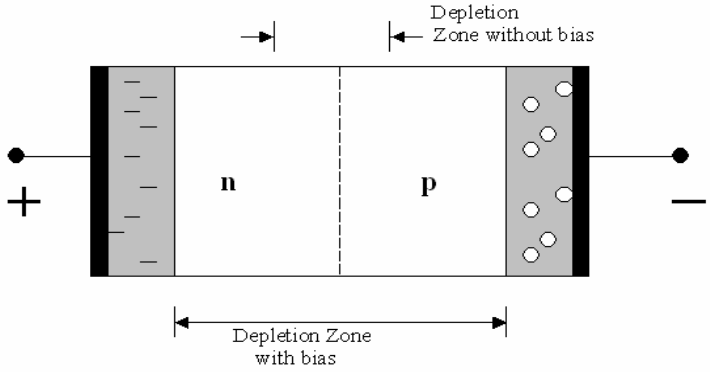

Figure 3.3: Reversed-bias junction.

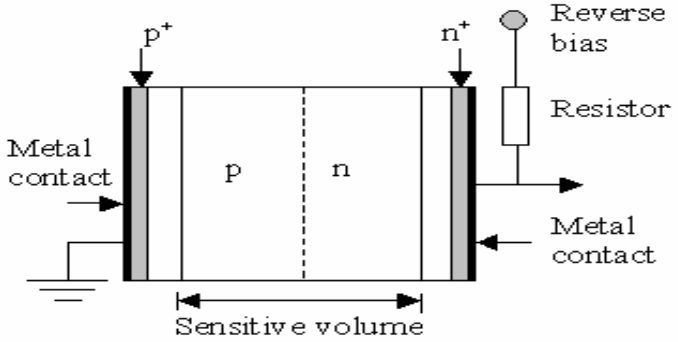

Figure 3.4: Basic configuration of a pn junction detector.

Electrodes are required on either side of the semiconductor, to collect charges. However, just depositing metal onto the semiconductor material cannot form metal contacts, because this creates its own depletion region into the semiconductor. To prevent this, an additional layer of heavily doped n^+ and p^+ are deposited between the metal and semiconductor material. The bias voltage to the detector is supplied through a series resistor for signal isolation purposes, as illustrated in figure 3.4. A charge sensitive preamplifier is used to collect the charge signal from the detector and the amplifier must have low noise characteristics.

The average energy required to create an electron-hole pair, at a given temperature, is very low in semiconductor detectors and is independent of the incoming radiation. In general, for Si and Ge at 77K, this energy is 3.81 eV and 2.96 eV respectively.

The response of the semiconductor is linear with the energy of the incoming radiation, if the depletion region is big enough to stop it. If E is the energy of the radiation and w is the average energy required to create an electron-hole pair, then E/w electron-hole pairs are created. The charge collected on the electrodes, Q, with a collection efficiency of n is given by

$$Q = \frac{nE}{w} e . \tag{3.20}$$

And the observed voltage is

$$V = \frac{Q}{C} = n \frac{E}{wC} e , \tag{3.21}$$

where C is the capacitance of the depletion region.

Since w is independent of the type of radiation, the response is linear with E and independent of the type of radiation. However, this is not true if the depletion region is not thick enough to stop the radiation. In this case the energy loss of the radiation is measured, instead of the energy of the radiation.

The energy resolution of the detector is dependent on the number of charge carriers and the Fano factor. The Fano factor, F, is a function of all of the various fundamental processes, which can lead to an energy transfer in the detector and has

values from 0 to 1. Better resolution is achieved with a small F. For both Si and Ge it is small and is about 0.12. The relative resolution, R, is

$$R = \Delta E / E = 2.35\sqrt{\frac{F}{J}} = 2.35\sqrt{\frac{Fw}{E}}, \tag{3.22}$$

Where ΔE is the energy resolution of the detector, E is the energy of the radiation and J is the number of electron–hole pairs created (E/w). $R \approx 0.07\%$ for Si.

A small fluctuating current, even though the reverse biased pn junction is nonconducting, flows through semiconductor junctions. This is called leakage current and appears as noise at the detector output. The leakage current has several sources, however, the largest source is through surface channels. In order to minimize this component clean encapsulation is generally required.

The intrinsic detection efficiency of semiconductors, for charged particles, is close to 100%. However, noise from the leakage current sets limit on sensitivity. For a given detector with a given cross-sectional area, the depleted volume contributing to detector noise, and hence the noise itself, is proportional to the depletion depth. Therefore the width of the depletion region must be carefully chosen so as to fully stop the radiation and that enough ionization is produced to form a signal larger than the noise level.

The output pulse shapes from semiconductors vary in rise time and form, because the collection time for electrons and holes depend on the location of the charges with respect to electrodes. Considering the simple pn junction detector formed from a p-type material, which is heavily doped on one side with n-type material. This would create a depletion region almost entirely into the p-side. Therefore

$$E = -\frac{eN_A}{\varepsilon} x, \tag{3.23}$$

where x is the position variable, ε is the dielectric constant, N_A is the impurity concentration and E is the electric field created. The conductivity of the junction is found to be $\sigma = eN_A\mu_h$. Substituting this would give

$$E = -\frac{\sigma}{\mu_h \varepsilon} x = -\frac{x}{\mu_h \tau}, \tag{3.24}$$

Where $\tau \equiv \varepsilon / \sigma = \rho\varepsilon$ and ρ is the resistivity. As shown earlier

$$v = \frac{dx}{dt} = -\mu_e E = -\frac{\mu_e}{\mu_h}\frac{x}{\tau}, \tag{3.25}$$

Which yields the solution

$$x(t) = x_0 \exp\frac{\mu_e t}{\mu_h \tau}. \tag{3.26}$$

The time it takes the electron to reach the electrode is then

$$t = \tau\frac{\mu_h}{\mu_e}\ln\frac{d}{x_0}. \tag{3.27}$$

And the charge induced during this period is thus

$$Q_e(t) = -\frac{e}{d}\int\frac{dx}{dt}dt = \frac{e}{d}x_0\left(1-\exp\frac{\mu_e t}{\mu_h}\right). \tag{3.28}$$

Similarly for the hole, we have

$$v_h = \frac{dx}{dt} = \mu_h E = -\frac{x}{\tau}, \tag{3.29}$$

Which yields

$$x(t) = x_0 \exp\frac{-t}{\tau}. \tag{3.30}$$

And the induced charge is

$$Q_h(t) = -\frac{e}{d}x_0\int\exp\frac{-t}{\tau}\frac{dt}{\tau} = -\frac{e}{d}x_0\left(1-\exp\frac{-t}{\tau}\right). \tag{3.31}$$

Here d is the depletion depth. The pulse shape is given by the total induced charge Q_{tot}, given by

$$Q_{tot} = Q_e(t) + Q_h(t) = -e. \tag{3.32}$$

The parameter τ determines the rise time of the pulse shape. The above calculation is for a single electron-hole pair. To find out the pulse shape due to ionization we need to know the particle trajectory, density of ionization along the track etc. Figure 3.5 shows a simulated charge pulse, integrated over 750 ns, including electron and hole contributions.

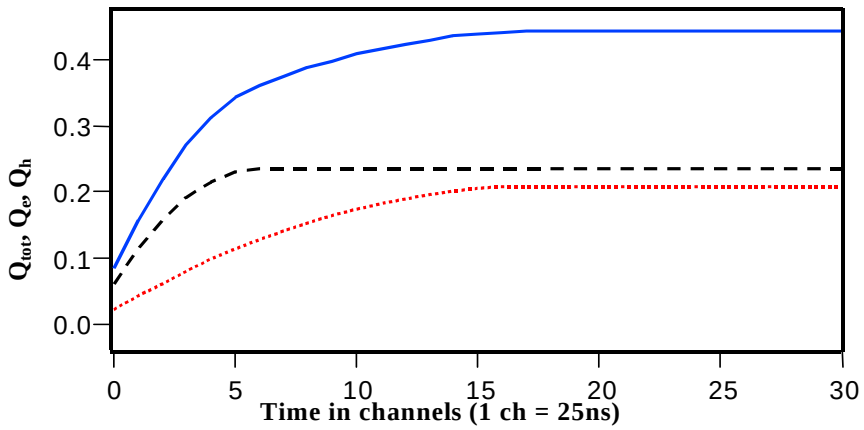

Figure 3.5: Simulated charge pulse including electron (dashed) and hole (dotted) contributions.

Semiconductor detector operation

The first thing to take care of is the bias voltage. Bias voltage determines the width of the depletion region and the capacitance of the detector and reduces the detector noise. However, too high bias voltage breaks down the detector. The bias voltage is supplied to the detector very slowly, in small steps of few volts, giving the detector time to settle before the next step. A good practice is to look at the detector noise signal in an oscilloscope while increasing the bias voltage. If a sudden increase is observed it could mean a break down. Typical bias voltage values for surface barrier detectors range from 50-300 V while that for germanium detectors range from 2000-5000 V.

Charge preamplification is an important stage in the detection scheme. Since the typical detector signals are very small, preamplifier and other electronics that follow the detector must have low noise characteristics. A charge sensitive preamplifier is used, because it is not sensitive to the variations in the semiconductor capacitance. Preamplifier capacitance is required to be much larger than the input capacitance to ensure stable operation. To minimize the preamplifier noise, the preamplifier input capacitance has to be small. This requires the preamplifier be mounted as close as possible to the detector. Coupling the preamplifier to the detector can be done directly, DC coupling, or through a capacitor, AC coupling.

The temperature effects are very important in detector operation. Temperature affects the conductivity of the semiconductor. It also increases the leakage current. Increasing temperature can also, at some point, result in detector break down.

Radiation damage is also an important effect to be considered. Incident radiation collides and knocks out the lattice atoms causing point defects. These structural defects result in discrete trapping levels in the forbidden band gap reducing the number of charge carriers in the semiconductor. Radiation damage increases the leakage current and degrades the energy resolution. It can also cause double peaks in the energy spectra. Sometimes increasing the bias voltage might compensate for the radiation damage.

The high density of electron-hole pairs created, for heavily ionizing radiation, leads to space-charge phenomena that affect the rise time and pulse height of the signal. The dense cloud of space charge along the particle trajectory reduces the applied electric field locally. This results in a higher collection time. The pulse rise time is therefore large and also during this delay some electrons may recombine with holes thereby reducing the total collected charge. This affects the energy resolution that can be achieved.

3.4 Bellows Electron Spectrometer for CARDS Array (BESCA)

BESCA stands for "Bellows Electron Spectrometer for CARDS array". It was constructed at Louisiana State University by Prof. E. Zganjar and used in several HRIBF (Holifield Radioactive Ion Beam Facility at Oak Ridge National Laboratory (ORNL)) experiments [Pie00, Bat03, Tan06]. It is a planar Si(Li) detector for conversion electron spectroscopy. Before discussing BESCA, a brief discussion on Si(Li) detectors is presented.

Lithium-Drifted Silicon Diodes – Si(Li)

The depletion region, which determines the response of the detector, has to be as thick as possible to achieve good detection efficiency. Ordinary pn junction detectors could not achieve depletion thicknesses greater than a few millimeters. To achieve greater thicknesses, semiconductor materials with high resistivities are required. This can be achieved by developing a compensated semiconductor material. A process called lithium-drifting can form the required compensated material.

Junctions formed with compensated material are called p-i-n junctions. These junctions have different properties than ordinary pn junctions. In particular, the compensated zone does not have space charge. This results in an almost constant electric filed in this zone.

Detectors made from lithium-drifted silicon are called Si(Li) detectors and they have a maximum depletion thickness of about 10-15 mm. They are suitable for β particle and low energy x-ray spectroscopy. Since the Si(Li) has a greater sensitive region, the noise contribution from thermally generated electrons and holes is much greater than in ordinary silicon diodes. Therefore to achieve high energy resolution Si(Li) detectors are required to be operated at low temperatures.

Besca detection system

The *Besca* detection scheme is based on a Si(Li) detector with a thickness of 5mm and ≈200 mm^2 area. The detector parts were made by ORTEC [ORT]. The detector entrance window has a gold layer with a thickness of about 20 nm. The detector and the preamplifier FET are operated at LN_2 temperatures. It is operated at a bias voltage of –500V. To ensure that there is no interacting medium between the source and the detector, vacuum pressure of about 10^{-7}Torr is created using turbo molecular vacuum pumps. To achieve very low noise, the vacuum pumps and vacuum chamber are isolated from preamplifier power. Also the amplifier is custom-soldered to the detector and shielded against noise pick-up. The energy threshold that can be achieved in experimental conditions can be less than 10 keV. The preamplifier signals are then collected using an acquisition system for analysis. An energy resolution as low as 0.8 keV (~1.3%) at 60 keV and 1.8 keV (~0.18%) at 975.7 keV can be achieved using this system. Figure 3.6 shows the experimental setup with BESCA for timing and pulse shape analysis. The test source used was ^{207}Bi. Two Si(Li) detectors were used, as explained later in chapter6, for timing and pulse shape analysis. Figure 3.7 shows the energy spectrum of ^{207}Bi decay obtained by BESCA. Figures 3.8, 3.9 and 3.10 show pictures of BESCA detection system at HRIBF.

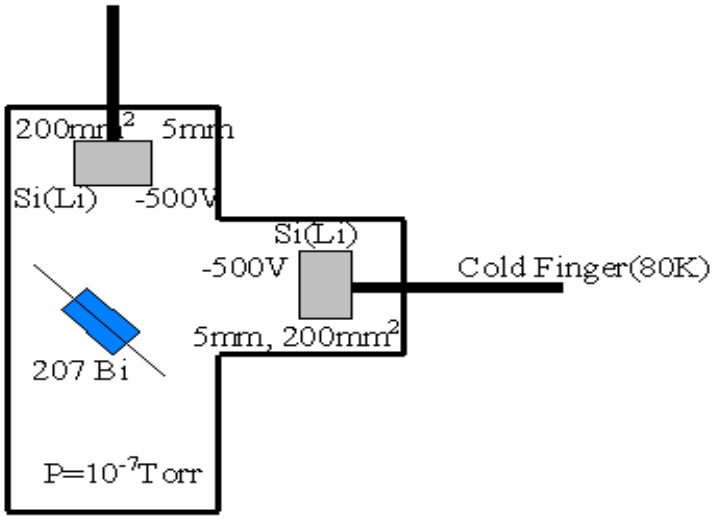

Figure 3.6: Experimental setup with BESCA for timing and pulse shape analysis.

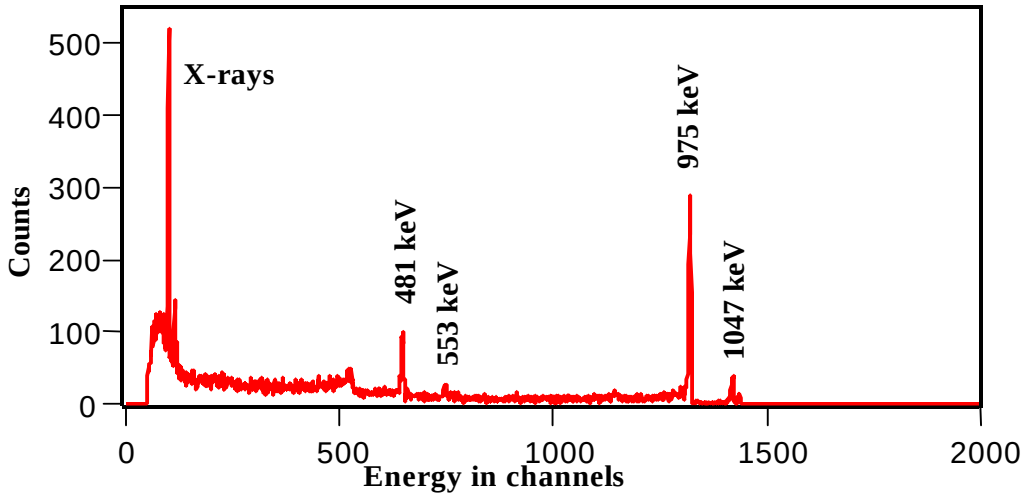

Figure 3.7: Conversion electron spectrum of ^{207}Bi using BESCA.

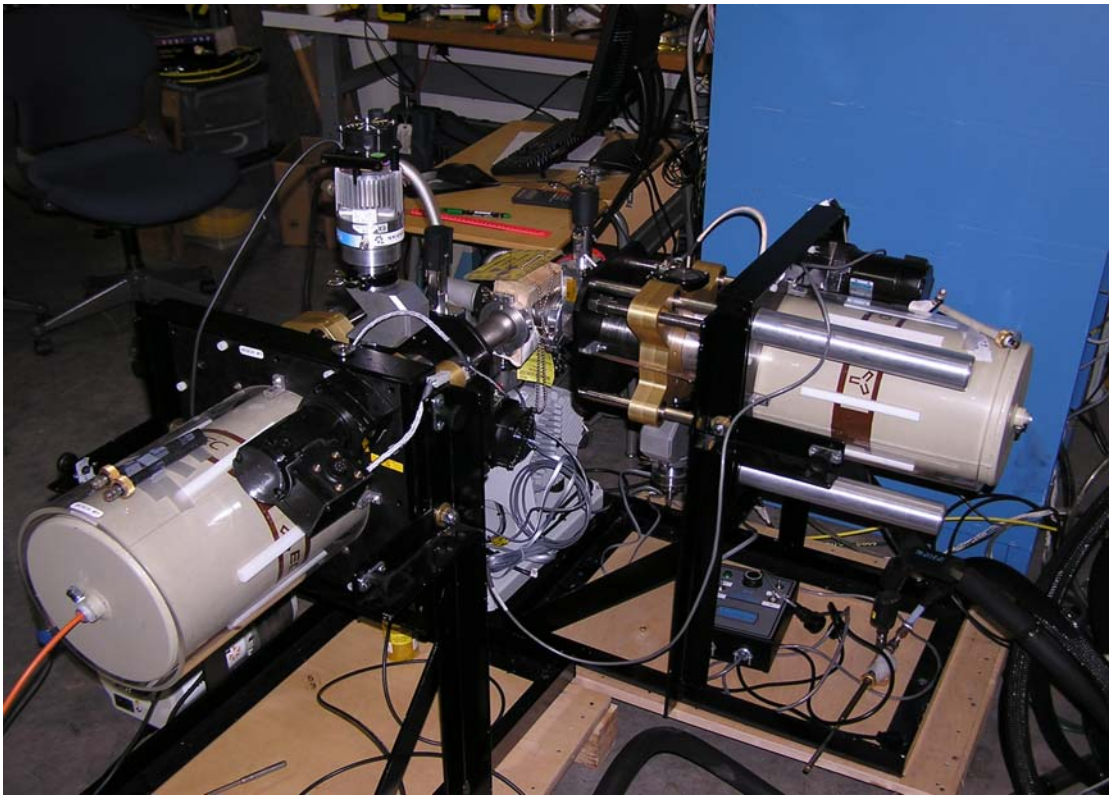

Figure 3.8: Experimental arrangement with two BESCA detectors.

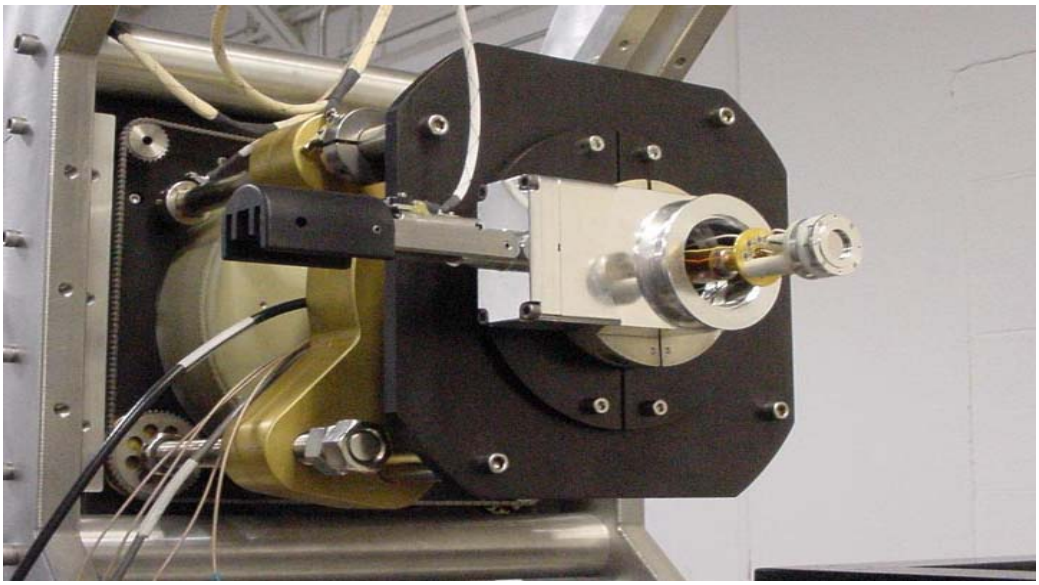

Figure 3.9: Si(Li) detector.

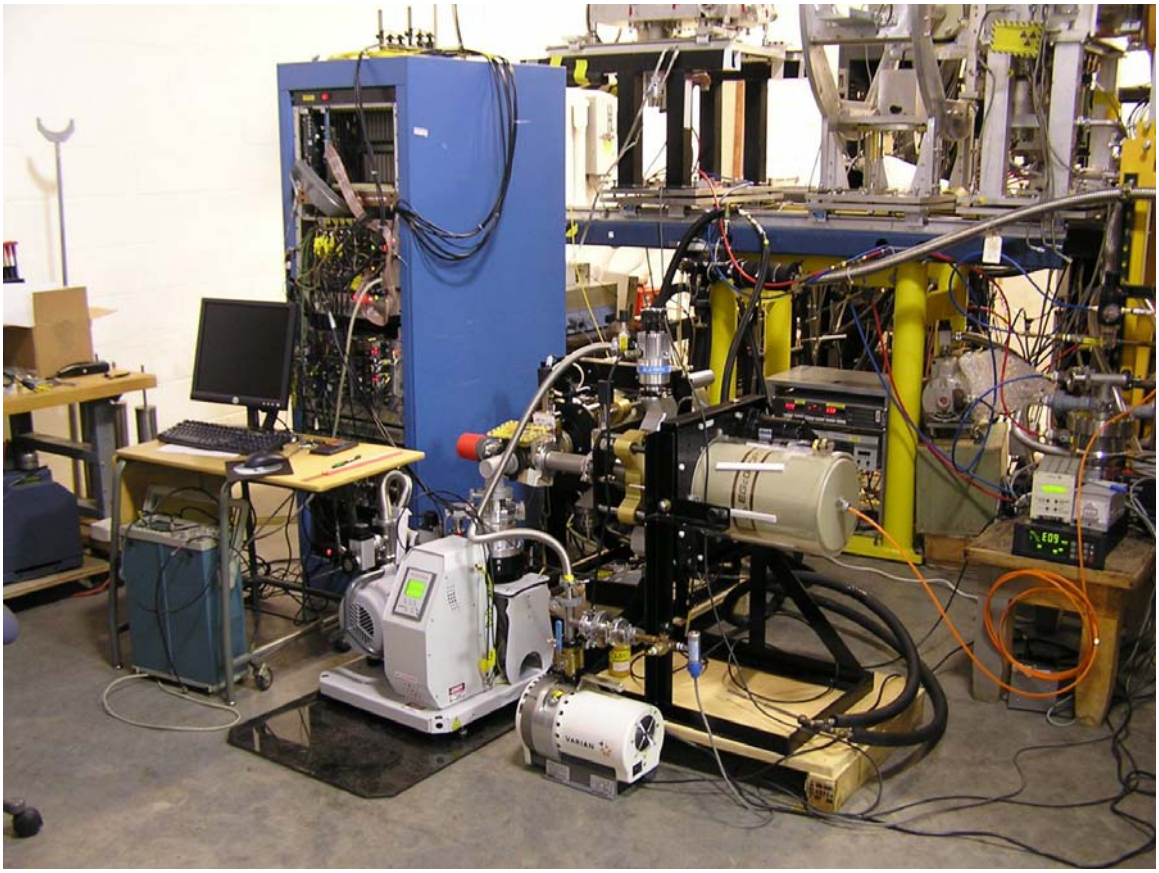

Figure 3.10: Experimental system with two BESCA detectors, data acquisition system and vacuum pumps.

Chapter 4

Digital electronics

The detection capabilities of the modern day nuclear spectroscopy tools have been increased with the application of data acquisition systems based on digital pulse processing (DPP). Energy and timing resolution equivalent or superior to the classic analog electronics based systems can be achieved. The appropriate real time numerical algorithms functionally replace transistor network based circuitry. In practice digital data acquisition systems enable researchers to employ flexible numerical algorithms in studies of nuclei with very short life times [Mom00, Grz03, Kar03, Lid06] or to achieve particle identification [Amm63, Pau94, Mut99].

In this chapter the digital data acquisition systems are discussed. First, the advantages of digital pulse processing (DPP) systems over traditional analog acquisition systems are presented, followed by a brief discussion of DGF4C and PIXIE16 digital data acquisition systems. Finally, some results from the commissioning of the PIXIE16 digital data acquisition system at HRIBF at ORNL are presented.

4.1 Analog and digital data acquisition systems

The task of a data acquisition system in experimental nuclear physics is to extract information of interest (pulse height, arrival time, pulse shape etc.), and to eliminate non-essential information (noise) and to reduce the incoming data stream to a manageable level. The difference between “analog” and “digital” data acquisition

systems will be discussed based on the example of typical systems serving a silicon detector.

A typical analog data acquisition system consists of charge preamplifier and pulse-shaping units with fast and slow branches. The task of the fast channel is to detect the time of arrival of the pulse and to produce a triggering pulse. The slow channel measures pulse amplitude. The signal in the slow channel is integrated and shaped (usually into a Gaussian) and its maximum amplitude is digitized using an analog-to-digital converter (ADC). Time differences between various detectors signals are measured using time-to-digital converters (TDC). The resulting numbers characterizing pulse amplitudes and time of arrival are transferred into a computer, which performs data analysis and storage.

A digital data acquisition system works schematically in a similar fashion, except that the signal is digitized immediately after the preamplifier stage by a fast sampling analog to digital converter and digital filters acting on the continuous stream of numbers carry out the functionalities of fast and slow channels. This way the "fast" and "slow" channels will work with the same identical copies of the pulse shape, dead time in digitizing is eliminated and signals can be analyzed immediately or after certain delay time without losing time information. An essential advantage of the digital data acquisition is the ability to stream the data through a first-in-first-out (FIFO) memory. This enables an arbitrary delay of the pulse without losing its fidelity, thus allowing time for digital filters to perform their functions on digital copies without the loss of information.

Typical digital and analog data acquisition systems are illustrated in figure 4.1
The advantages of a typical digital data acquisition system can be listed as follows:

- It can store more complete information about the pulse, including the digital image itself.
- It can be adjusted and upgraded to the changes in experimental situation in software. The improvements can be easily implemented.
- It is very stable, because the signal digitizing is done early and then it is immune against electronic noise or temperature fluctuations.

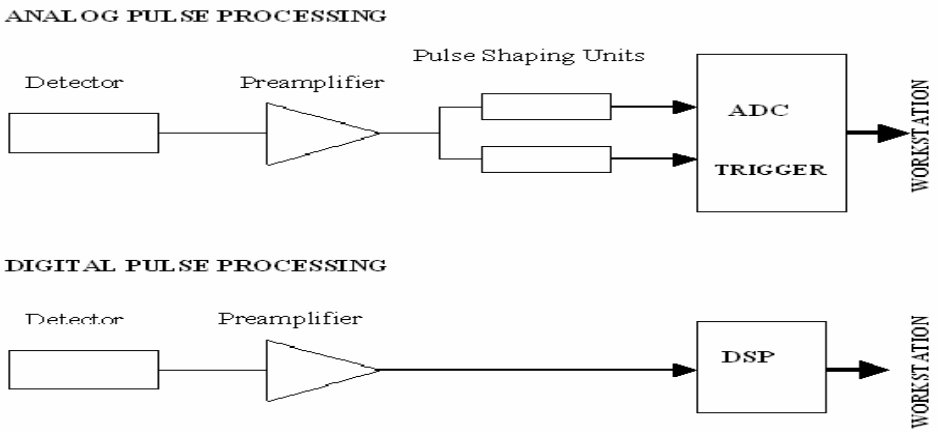

Figure 4.1: Block diagrams for analog and digital pulse processing units.

- The DSP based systems already have proven equivalent functionalities to analog systems for energy and time measurements.
- Two most important demands in nuclear spectroscopy, low electronic threshold and good timing resolution, are satisfied with digital electronics.

An example of efficient approach for Digital Pulse Processing (DPP) implementation has been developed by XIA corporation and applied by several groups in the nuclear spectroscopic studies [Hub99, Grz03]. Their approach, developed to provide high throughputs, divides the filtering action into two steps. In the first step, a Real Time Processing Unit (RTPU) processes the input amplifier signal at an ADC rate much like the fast channel in the analog system. In the second step, signal values from RTPU are processed at event rate by a DSP.

DGF4C, a digital data acquisition board developed by XIA corporation, has been used at HRIBF at ORNL for several years [Grz03]. In the last three years, PIXIE16, a new generation digital board which implements concepts similar to DGF4C but with more functional capabilities, has been commissioned at HRIBF. These data acquisition systems have enabled researchers at HRIBF to study exotic and very short-lived nuclei much more effectively. In these applications the DGF4C based systems were enabling measurements difficult or impossible to perform using analog electronics, for example

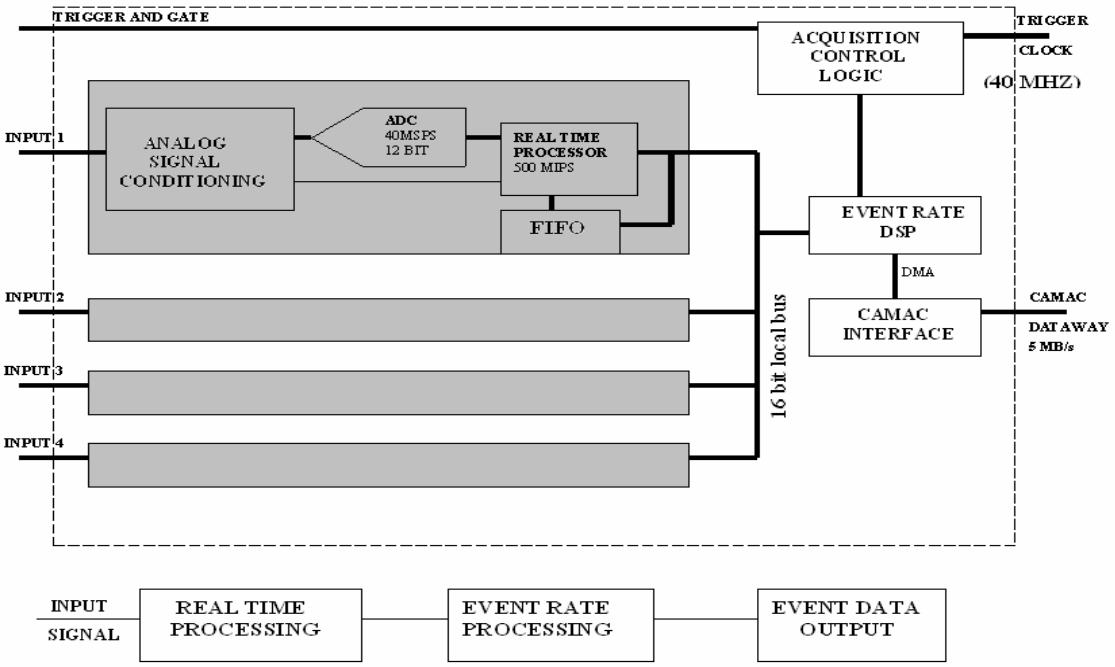

Figure 4.2: DGF4C functional block diagram, as presented in [XIA04, Grz03].

when the measurement of closely overlapping pulses from short lived radioactivities, was required as in case of detection of proton and alpha radioactivities [Kar03, Lid06]. The DGF4C functional block diagram and its internal architecture [XIA04, Grz03] are shown in figure 4.2. DGF4C is a single width CAMAC board featuring four signal input channels. It incorporates four different building blocks: Analog signal conditioner (ASC), Real-time processing unit (RTPU), Digital signal processor (DSP) and CAMAC interface. Each channel is comprised of ASC, ADC and RTPU.

Analog signal conditioning (ASC)

Each channel of the DGF4C has its own conditioning unit. The purpose of this unit is to bring the input signals into the voltage range of the 12-bit ADC, whose range is 0-1V, that follows this unit. Also the signals are adjusted for DC offsets. User can control the gain of the amplifying stage through computer interface.

Analog-to-digital converter (ADC)

The ADC is a waveform digitizer sampling at 40MHz. In the case of DGF4C board it is based on the 12 bit AD9042 chip manufactured by Analog Devices.

Real time processing unit (RTPU)

Each channel has an RTPU, which is comprised of a Field Programmable Gate Array (FPGA) and a first-in first-out (FIFO) memory. RTPUs apply digital filters to the incoming signal, from the ADC, to perform the same operation as a shaping amplifier. Finite impulse response (FIR) filters are typically used and DGF4C RTPUs use a "trapezoidal" filter, whose parameters can be controlled by the user.

Another component of an RTPU is a pile up inspector. If a second pulse occurs too soon after the first, this would corrupt the pulse height measurement of the first pulse. The logic of the pile up inspector ensures that these two pulses are rejected as pile up. However if the pile up occurs on the rising edge of the first pulse, the pile up inspector would treat them as a single pulse and would pass the inspection. Therefore the pulses have to be separated at least by their rise time to be effectively recognized as pile up. If a pulse was detected and passes the pile up inspection, a trigger signal is issued. This would notify the DSP that raw data is available. When a trigger is generated the raw data is latched, hold, until the DSP services the RTPU.

The third component of the RTPU is a FIFO memory, which is controlled by the pile up inspection logic. The FIFO memory will be continuously filled with waveform data from the ADC. On a trigger it is stopped and the read pointer is positioned to the start point of the pulse, which caused the trigger. When the DSP collects data, it can read any fraction of the stored waveform, up to the full length of the FIFO.

Digital signal processor (DSP)

The DSP controls the operation of the DGF4C. It reads raw data from RTPUs, reconstructs true pulse heights, applies time stamps, prepares data for output to the host computer and increments spectra in its on-chip memory. The host computer communicates with the DGF via the CAMAC interface.

The user, through the host computer, sets variables in the DSP memory and calls DSP functions to program the hardware. Through this all gain and offset DACs are set and RTPUs are programmed this way. Once set up, the RTPUs process their data without support from the DSP. When one or more RTPUs generate a trigger, an interrupt request is sent to the DSP. It responds by reading the required data from the RTPUs and storing them in memory. It then returns from the interrupt routine without processing the data to minimize the DSP induced dead time.

In this way, RTPUs have more processing power. Each RTPU takes incoming waveforms from its associated ADC in real time and produces, for each valid event, a set of distilled data from which pulse heights and arrival times can be reconstructed. The computational load of the DSP is very much reduced this way, as it has to react only on event-by-event basis and has to work with only a small set of numbers for each event.

In addition, the DSP code for DGF4C has been modified for customized applications at The University of Tennessee (UT). The onboard DSP reads raw energy filter values and up to 100μs of pulse waveforms. In basic DSP code, the length of the waveform is the same for all events. In contrast, the modified DSP code checks the energy of a detected pulse, and if larger than a threshold (user defined), reads out only the energy and timestamp. If smaller, it also acquires a waveform. Thus the data transfer rate to the host computer is much reduced as only pulses of interest are acquired in full detail. This function is implemented in the DSP board by estimating the energy of a pulse from the difference of the raw energy filter sums before and after the leading edge of the trigger.

CAMAC interface

The CAMAC interface through which the DGF4C communicates with the host is implemented in its own FPGA. The interface conforms to the regular CAMAC standard with a cycle time of 400ns per read operation. The interface moves a 16-bit word at a time.

Data can be acquired in two modes. One is the MCA histogram mode and the other one is the list mode. The *MCA histogram mode* is used if only the spectra of the data

are desired. For each event, the pulse height is calculated and used to increment the spectrum for the corresponding channel, then discarded. Runs can continue indefinitely, or until a preset time is reached. Run statistics are available, along with the spectrum, after the run. The *list mode* is used if it is desired to collect data on event-by-event basis, gathering energies, time stamps, pulse shape analysis values and waveforms. In list mode, energy spectra are also obtained for monitoring purposes. Runs will continue until the output buffer is filled, or a preset number of events are reached. The control software also includes a timeout feature, which causes the user to end runs that do not end themselves.

Control Software

The DGF4C is controlled by computer control software called IGOR, developed by Wavemetrics Inc. IGOR provides an interactive software environment for scientific experiments. IGOR can be used for data acquisition and analysis. It allows users to write their own analysis functions with its built-in programming environment, which is similar to C. IGOR allows users to create a customized interface for controlling a hardware component or for achieving any other task. IGOR can handle large data sets and data can be imported into IGOR in many ways. A DGF4C sends data to IGOR as a binary data file. Data are stored in IGOR as waveforms. It also has several built in scientific analysis functions. It can also be extended for its features and operation by users with their own C/C++ codes using an external operation toolkit, called an XOP.

To control DGF4C, a customized interface, data acquisition, analysis and filtering software was developed by XIA corporation using IGOR. This software can be modified to achieve desired functionality. Figure 4.3 shows a snapshot of IGOR running on a computer using the Windows XP operating system.

4.2 PIXIE16

Pixie 16 is a significantly enhanced digital board, which follows the general concepts as described above for the DGF4C board. Pixie16 features improved functionalities. It has 16 input channels as opposed to 4 input channels with DGF. The

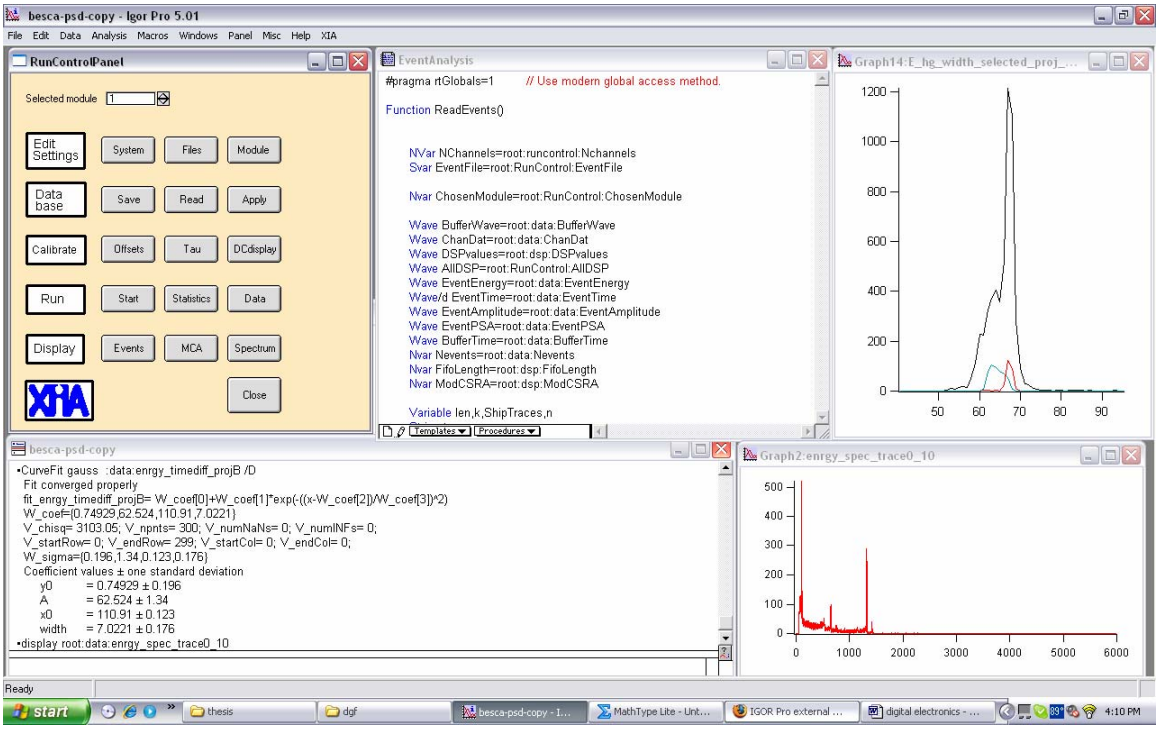

Figure 4.3: A snapshot of IGOR running.

ADC sampling frequency is 100 MHz, which is much faster than the 40 MHz of the DGF. Pixie can store traces of lengths up to 10,000 samples while DGF can accommodate 1000 samples. Pixie 16 can achieve data transfer rates of up to 40MBPS because it is implemented into a modern cPCI standard while CAMAC based DGF can only achieve 2 MBPS. Also, Pixie 16 has 64 bit local data bus lines as compared to 16 bit local bus lines of DGF. All these improvements enable a much faster and more efficient digital data acquisition. The functional block diagram of Pixie16, as presented in [Pix04, XIA], is shown in figure 4.4.

Pixie16 follows the same basic functional principle as that of DGF4C. Almost all the sub-components are grouped around the local data bus. Each signal processing FPGA (SP-FPGA) accepts inputs from four ADCs. The FIFO memory, used for pulse shape acquisition, is implemented in the SP-FPGA itself. The FIFO can store trace lengths of up to 10,000 samples for each of the four channels.

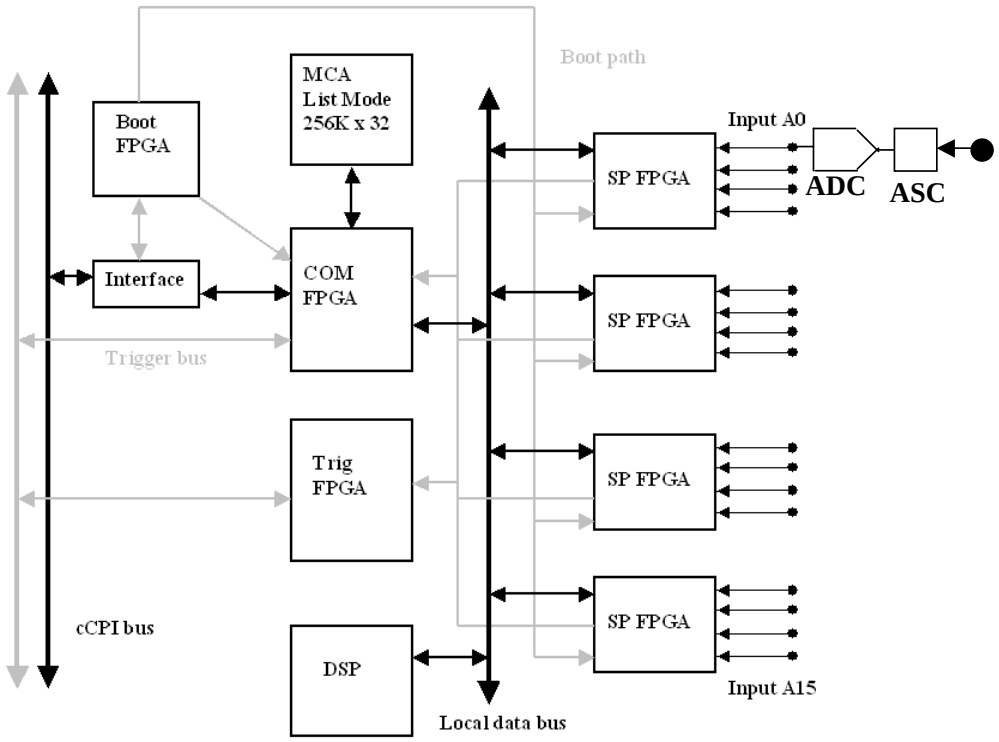

Figure 4.4: Pixie16 functional block diagram, as presented in [Pix04, XIA].

The DSP has access to all FPGAs, as in DGF, and receives processed data from them. The DSP accesses the local data bus using 64 parallel data lines, which maximizes the data transfer rate. The SP-FPGAs also put their data on local data bus as 64 bit words. List mode data is stored on the large on-chip memory of the DSP. Histogram memory is provided external to the DSP, as opposed to the internal histogram memory for DGF. A communications FPGA (COM-FPGA) is used by the DSP to access the histogram memory. The total histogram memory is 256Kx32-bit words, which means each of the 16 input channels has 16K memory for its spectrum.

The trigger FPGA (Trig-FPGA) controls the triggering action. Pixe16 runs two clocks. One is a 40 MHz clock, which gets doubled to 80 MHz by the DSP and is only used by the DSP. The other is a 50 MHz clock, which is distributed between modules and is used to synchronize all the time sensitive operations. This clock gets doubled to 100 MHz on each Pixie16 board. The clock is distributed to modules via the cPCI back

plane. The trig-FPGA connects the locally generated trigger and synchronization signals to the remotely generated back plane signals. Trigger-FPGA routes and processes trigger data, creating a rich set of triggering capabilities.

Pixie16 uses a 33MHz, 32-bit compactPCI computer interface (cPCI). This can achieve data transfer rates of up to 100 MBPS (achieved so far only 20MBPS due to limitations in the board architecture) when reading histogram data and also about the same rates when reading the list mode data.

The analog chain for each input of the Pixie16 has two operational amplifiers, a digital-to-analog converter (DAC) and an analog-to-digital converter (ADC). The first amplifier provides a gain of 21. Any DC-offset of the signal can be compensated for with a 16-bit DAC. The second amplifier acts as an anti-aliasing filter and has a gain of 2. The total gain is, therefore, 42. The ADC sampling frequency is 100 MHz with a range of 2V. Therefore the dynamic range of the analog chain is 48 mV.

4.3 Commissioning of Pixie16 prototype at HRIBF

Recently, a new and improved data acquisition system based on Pixie16 was developed at The University of Tennessee in collaboration with HRIBF at ORNL. The commissioning process started with testing the performance of the Pixie16 prototypes. At first, the pulse height measurement resolution as a function of filter parameters was investigated using signals from a pulse generator and a ^{137}Cs source. The High Purity Germanium Detector (HPGe) has been used, for these measurements. The signal properties for this semiconductor detector are very similar to that of BESCA, but its advantage is a greater ease of use. The optimal filter parameters such as the filter "peaking" and "gap" times (explained in detail in chapter6) and pulse decay constant (τ) were identified to achieve best energy resolution as reflected by the Full Width at Half Maximum (FWHM) of the energy peak in the measured spectrum.

While testing for the resolution against different peak times of the energy filter, we have identified a problem with the analog conditioning circuitry of Pixie16 boards and the cPCI chassis power supply. It was determined that both components were

leaking electronic noise around 0.5MHz frequency into the signal processing circuitry, thus significantly degrading the quality of the signal.

The problem manifested itself during the attempt to optimize the digital filters; unexpectedly, while increasing the integration time of the filter ("peaking" parameter) we observed a degradation of the energy resolution instead of improvement, as evidenced by the red points in figure 4.5. The expected resolution of about 0.25% for the HPGe detector could not be achieved. Such behavior would essentially eliminate that version of Pixie16 from application in high-resolution gamma ray spectroscopy. The boards and chassis were returned to the vendor for improvements, and significant modifications, including adding analog filters to the responsible signal conditioning units and replacement of the power supplies, were made by XIA. Figure 4.5 shows a plot of resolution against peak time of the energy filter before and after the problem was corrected. The optimizations and further tests reported here were performed on the modified version of the Pixie16 board.

By checking all the values the optimal filter parameters were found to be $1.04\mu s$, $0.64\mu s$ and $59.69\mu s$ for peak time, gap time and τ respectively. With these filter parameters the Pixie16 is tested for best resolution (FWHM) achievable with ^{152}Eu source with a low-energy photon gamma ray detector (LOAX) detector, as illustrated in figures 4.6 and 4.7. These results are then compared to the resolution achieved with the DGF. Pixie16 achieved a resolution (FWHM) of about 0.29% and is close to the resolution achieved by the DGF, see figure 4.8, which is about 0.24%.

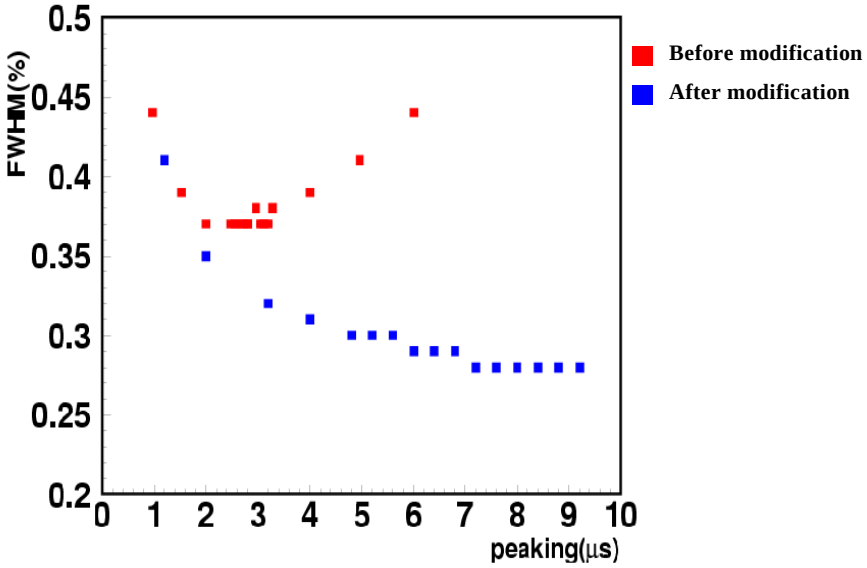

Figure 4.5: Plot of resolution (FWHM in %) against peak time of the energy filter before and after the modification of signal conditioning unit and power supply of Pixie16. The tests were performed using the ^{137}Cs Source.

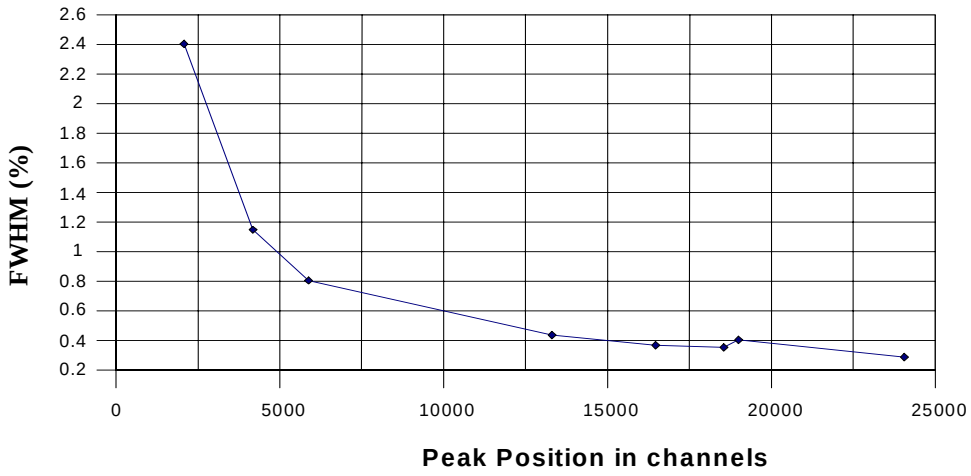

Figure 4.6: Peak position Vs FWHM for Pixie16 with ^{152}Eu source for the high gain input of Pixie16. The best resolution achieved is 0.29% for the 1408 keV line.

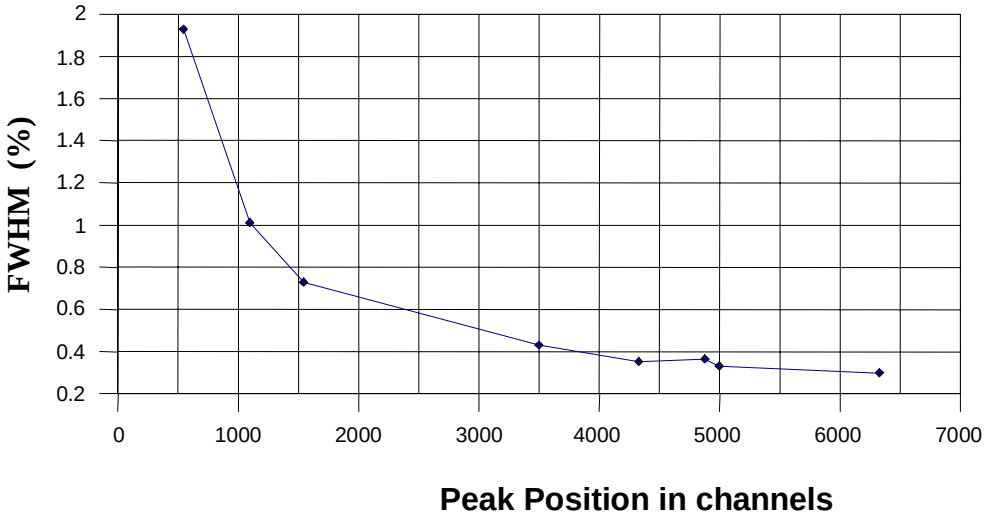

Figure 4.7: Peak position Vs FWHM for Pixie16 with ^{152}Eu source for the low gain input of Pixie16. The best resolution achieved is 0.3% for the 1408 keV line.

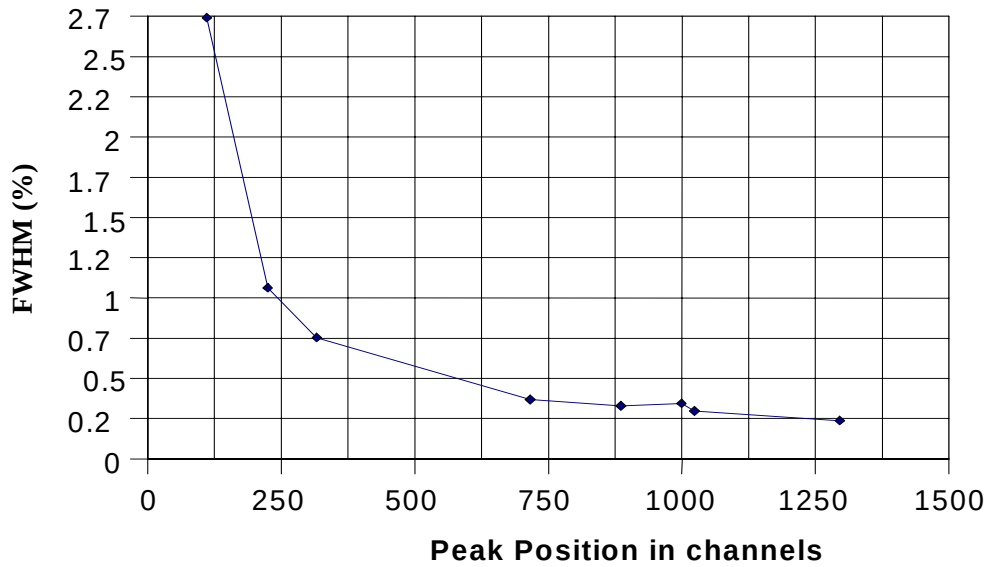

Figure 4.8: Peak position Vs FWHM for DGF with ^{152}Eu source. The best resolution achieved is 0.24% for the 1408 keV line.

Chapter 5

Simulated pulse shapes for Si(Li) detector

In order to apply pulse shape discrimination techniques, it is necessary to understand the electronic pulse generation process in the semiconductor detector. Using the interaction mechanisms of electrons and gamma rays with matter and charge collection processes in a semiconductor, as discussed in previous chapters, the pulse shapes from an appropriate Si(Li) detector design have been simulated. These pulse shapes are then analyzed to develop algorithms to discriminate between different kinds of radiation, which interact in the detector. We will demonstrate a technique, which will enable differentiation between gamma rays and high-energy electrons interacting with the detector material. Electrons impinging on a detector crystal interact continuously, along the primary electron track, whereas γ-rays interact predominantly through Compton scattering, which induces very localized charges. Schematically the developed algorithm will seek to differentiate between point-like (γ-rays) and continuous (electrons) interactions with the detector material. Figure 5.1 shows a schematic illustration of electron and γ-ray interacting with a detector medium.

A planar semiconductor detector can be thought of as a plane (parallel plate) capacitor. When an electron or a γ-ray interacts with the detector medium, it creates electron-hole pairs in the medium. These pairs are collected on the two surfaces (plates) of the detector as a result of an applied electric field. For the planar Si(Li) detector, a detector bias creates constant electric field across the detector medium, as described in chapter 3. Electrons, being negative charge carriers, travel towards the positively charged surface and holes travel towards the negatively charged surface.

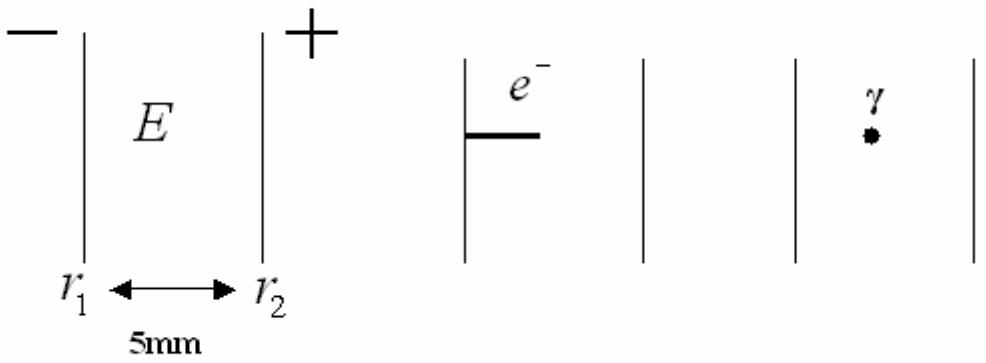

Figure 5.1: Si(Li) detector, schematic electron and γ-ray interaction with the detector medium.

Ramo-Shockley theorem

Ramo [Ram39] and Shockley [Sho38] independently found a method to calculate the total charge induced by a moving charge q on an electrode of a vacuum tube. The method originally developed for the system without space charge as explained in [Zho01], later it was generalized [Jen41, Cav71] for applications to detectors, which have stationary space charge.

The Ramo-Shockley theorem, as explained in [Zho01], states that the charge Q and current I induced on an electrode by a point charge q moving with velocity v are given by

$$\begin{aligned} Q &= -q\varphi_0(x) \\ I &= qv \cdot E_0(x)' \end{aligned} \tag{5.1}$$

under the conditions that the selected electrode is at unit potential, all other electrodes are at zero potential and all other charges are removed. Here $\varphi_0(x)$ and $E_0(x)$ are the electric potential and field that would exist at q's instantaneous position x, respectively. φ_0 and E_0 are also called the weighting potential and the weighting field, respectively. With charge q moving in space from x to $x+dx$, the change in induced charge is

$$dQ = q*dx*E(x). \tag{5.2}$$

The total induced charge can be found by integrating dQ over the collection time.

As explained previously, the incoming radiation liberates electron-hole pairs in the detector, which then drift towards the detector surface. In order to simulate the pulse shapes generated by the incoming radiation one has to know the total induced charge on the detector plates, induced by electrons and holes. We use the Ramo-Shockley theorem to calculate the induced charge. By knowing the change in induced charge, we can then calculate the induced current.

Pulse shape simulation algorithm

The Si(Li) detector simulated here is 5mm thick with a constant reverse bias voltage of V=500V. The simulation algorithm is as discussed below.

- The constant bias voltage V_b and the resulting constant electric field given by $E = \frac{V_b}{(r_2 - r_1)}$ are defined.
- The mobilities of the electrons and holes, μ_e and μ_h respectively, are defined as μ_e=3.1x10^4 cm^2/(V.s) and μ_h=1.1x10^4 cm^2/(V.s).
- For different interaction points, 10 evenly spaced points over 5mm thickness, the charge distributions are calculated for both continuous (e^-) and point like (γ) interactions.
- Velocities of electrons and holes in the electric field E are found using v = μE.
- Using *Ramo-Shockley* theorem, the total induced charge on the detector plates is found as

$$Q = \int E(r) v q dt \,. \qquad (5.3)$$

The induced current $I = \frac{dq}{dt} = \frac{\Delta q}{\Delta t}$ is also calculated.

This is done at both ends of the detector plates, that is for both electrons and holes.

- The pre-amplifier response function is defined as discussed in [Mih01]. It is given by

$$f(t) = \frac{Amp}{\left(T_d - T_r \frac{\sqrt{\pi}}{2\sqrt{1.3}}\right)}\left[\exp\left(-\frac{t}{T_d}\right) - \exp\left(-\frac{1.3t^2}{T_r^2}\right) + osc\right]. \qquad (5.4)$$

Here *Amp* is the amplitude of the pulse and T_d and T_r are the decay and rise times (pre defined). *osc* is a damped oscillator function added to simulate the oscillatory action of the pre-amplifier circuits such as an RC circuit.

- The voltage signal, folded with the response function of the pre-amplifier, is then given by

$$V = \int I(t) f(t - t')dt' . \qquad (5.5)$$

- The voltage signal is then sampled to simulate the action of analog-to-digital converter (ADC).

Figures 5.2 to 5.7 show the simulated pulse shapes using the above-mentioned algorithm.

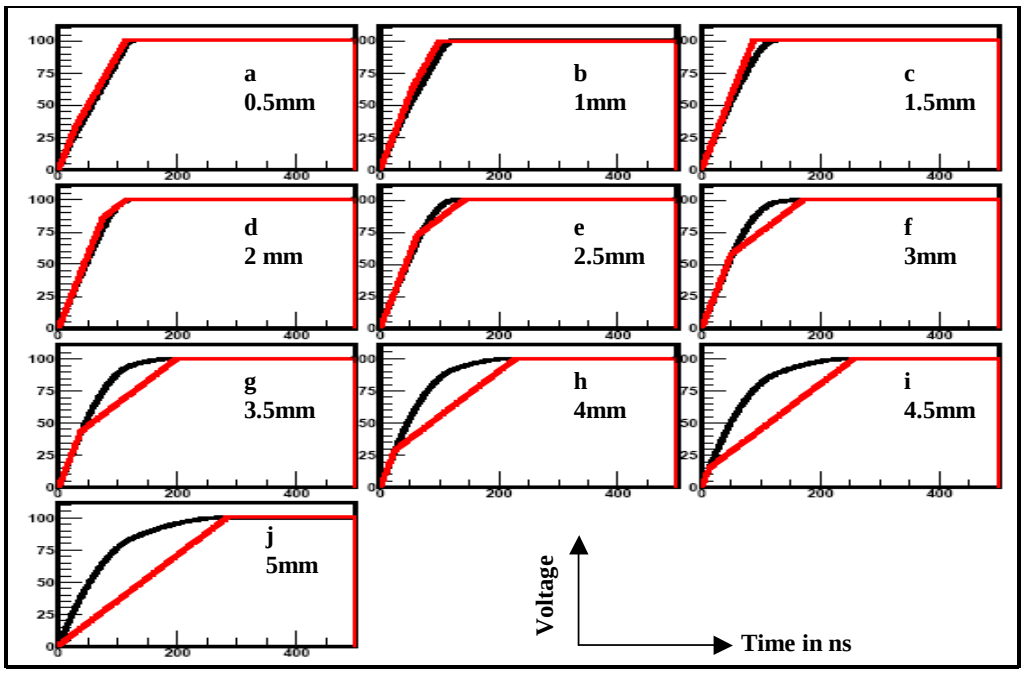

Figure 5.2: Calculated induced voltage on the detector plates, for continuous (black) and point-like (red) interactions, at different depths of interaction.

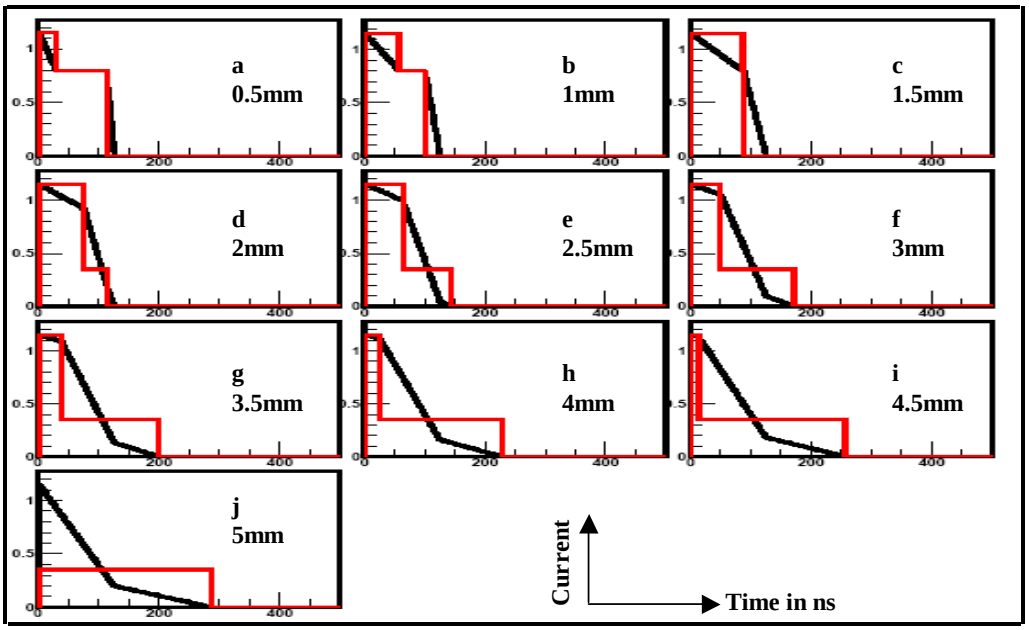

Figure 5.3: Calculated induced currents on the detector plates, for continuous (black) and point-like (red) interactions, at different depths of interaction.

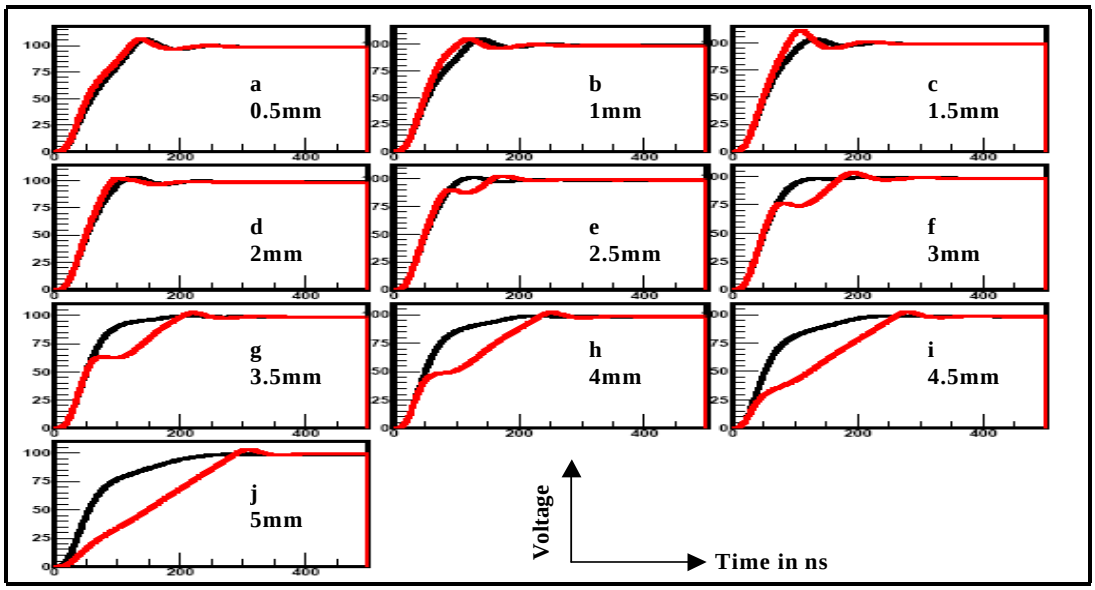

Figure 5.4: Calculated voltage signals folded with pre-amplifier response function, for continuous (black) and point-like (red) interactions, at different depths of interaction.

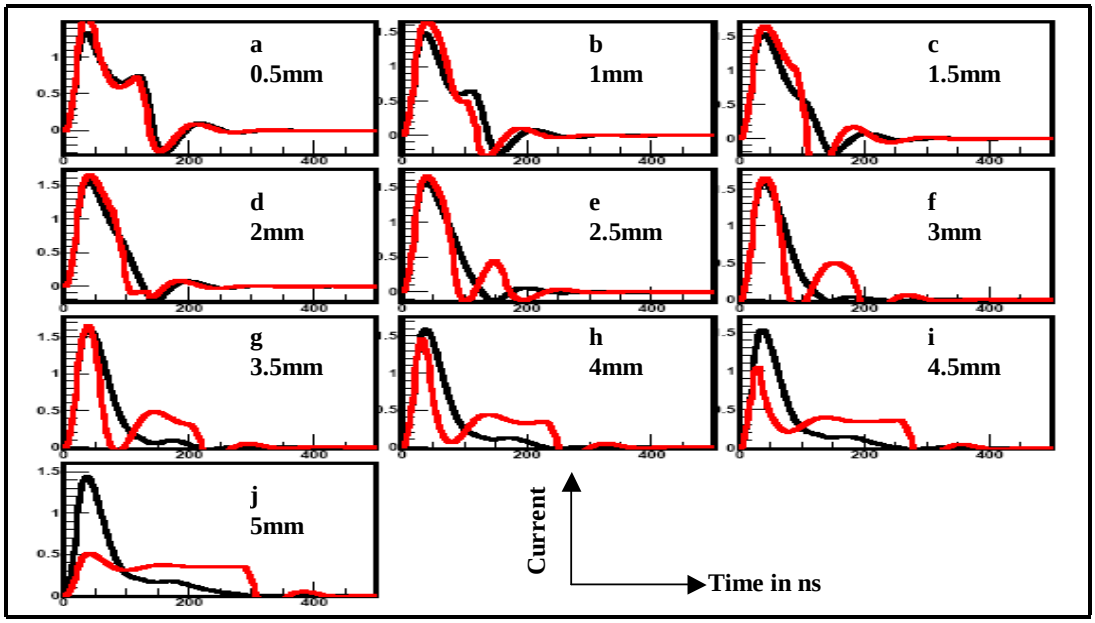

Figure 5.5: Calculated current signals folded with pre-amplifier response function, for continuous (black) and point-like (red) interactions, at different depths of interaction.

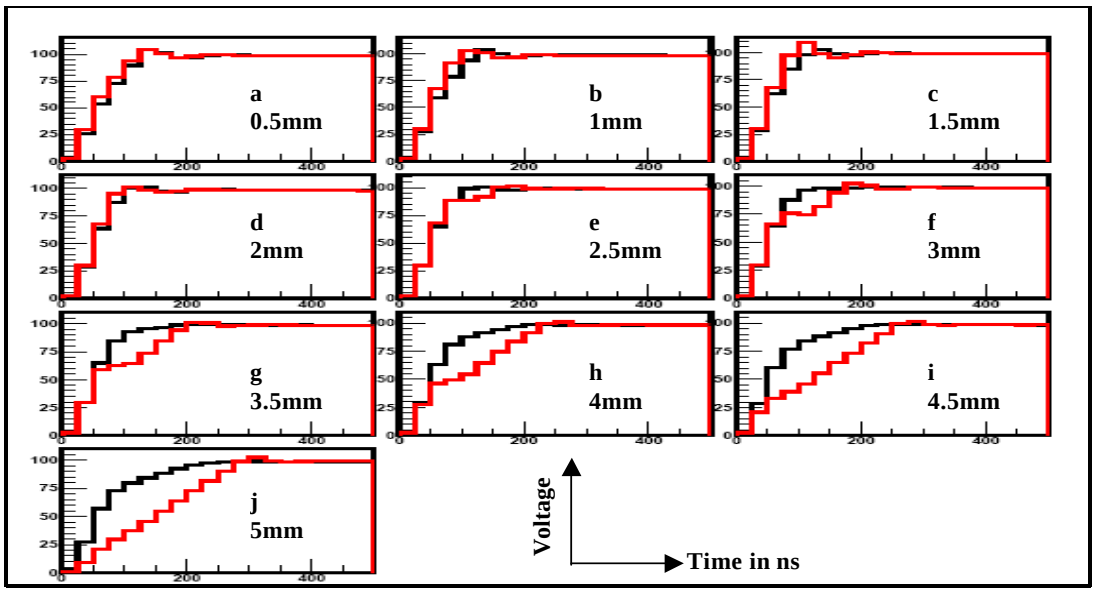

Figure 5.6: Calculated voltage signals folded with pre-amplifier response function and sampled, for continuous (black) and point-like (red) interactions, at different depths of interaction.

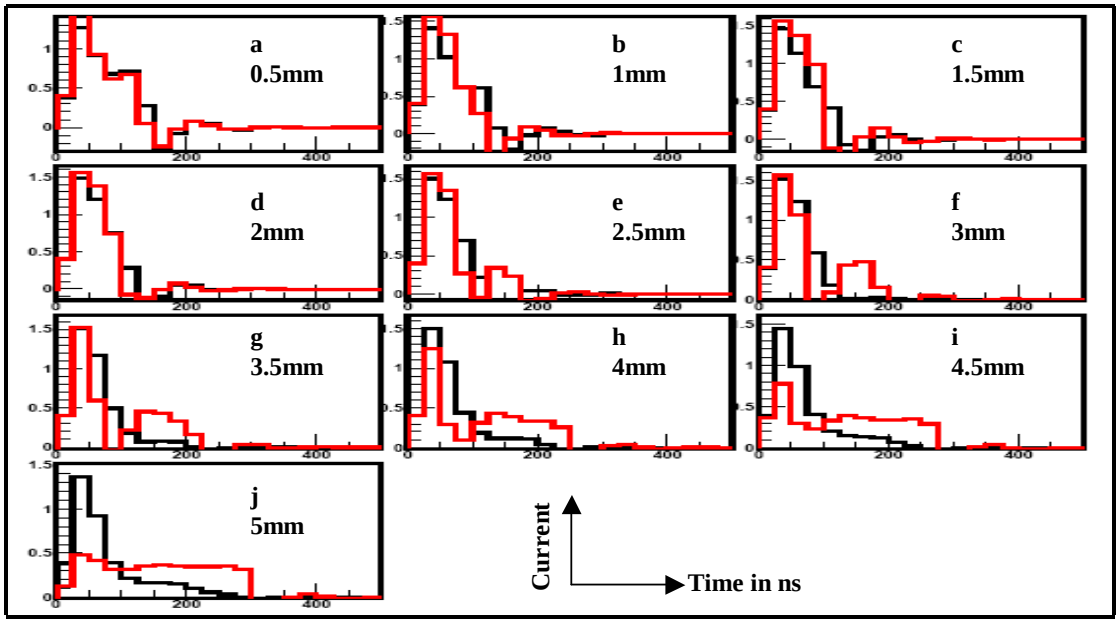

Figure 5.7: Calculated current signals folded with pre-amplifier response function and sampled, for continuous (black) and point-like (red) interactions, at different depths of interaction.

Figure 5.3 most strikingly represents the difference between the electron and gamma ray induced currents on one of the detector plates. The pulse shape discrimination algorithm utilizes these differences between time dependent current distributions. For a gamma ray, which interacted once in a detector through a Compton scattering event, the localized induced charge distribution can be approximated to be point-like. The resulting induced current due to the drift of the electrons and holes towards respective electrodes is constant and charge collection is determined by the drift velocities of negative and positive charge carriers. Hence the resulting current distribution consists of two "rectangles", where the length of each rectangle is determined by charge collection times.

For continuously ionizing particles (electrons) the induced charge is distributed along the particle track and hence the charge collection is also determined by the carriers drift times. But because the charge drift can be imagined as a movement of the "charge column" rather than the point, the resulting distribution has a shape of the sum of a

trapezoid and a triangle. The task of the effective discrimination algorithm is to be able to extract these differences from the measured pulses. Figures 5.6 and 5.7 show voltage pulse and its numerical derivative (current) for the realistic simulation, which employs the integrating charge preamplifier's response function and the action of the 40 MSPS digitizer. It is clear that key discriminating features of the pulse shape are preserved. Figures 5.8 and 5.9 show sample voltage pulses induced by an electron and a γ-ray from experiment. Figures 5.10 and 5.11 show the rising edges of figures 5.8 and 5.9 respectively. Figure 5.12 shows sample current pulses, from experiment, by an electron and a γ-ray.

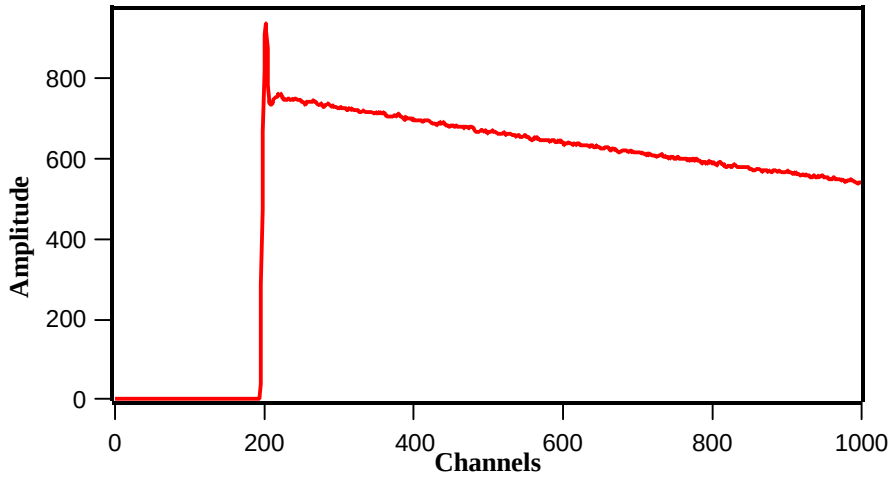

Figure 5.8: Sample electron pulse from the experiment.

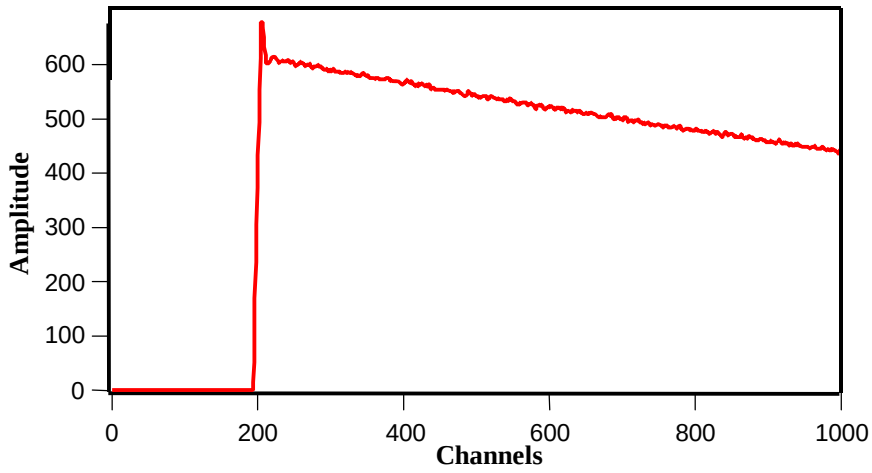

Figure 5.9: Sample gamma pulse from the experiment.

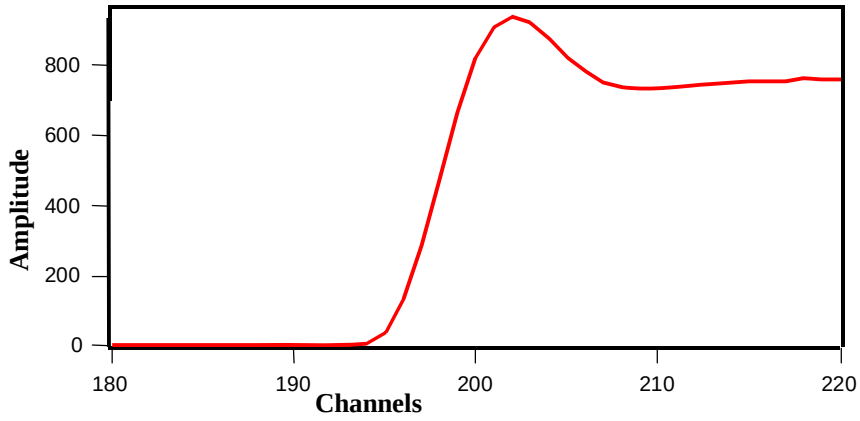

Figure 5.10: Sample electron pulse (rising edge) from experiment.

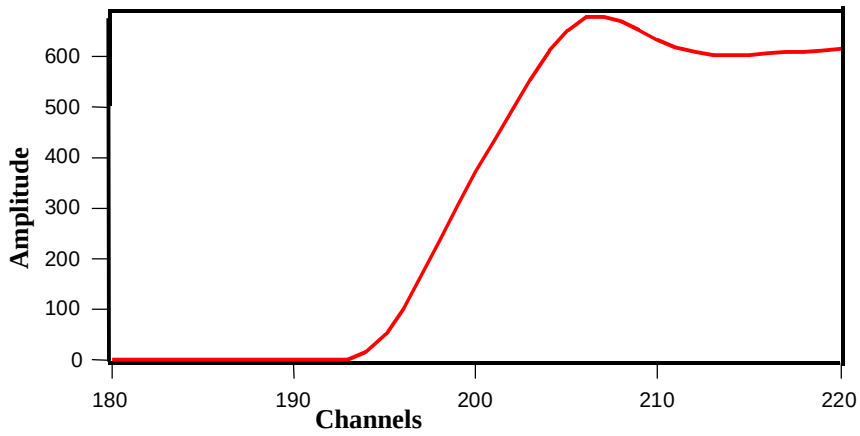

Figure 5.11: Sample gamma pulse (rising edge) from experiment.

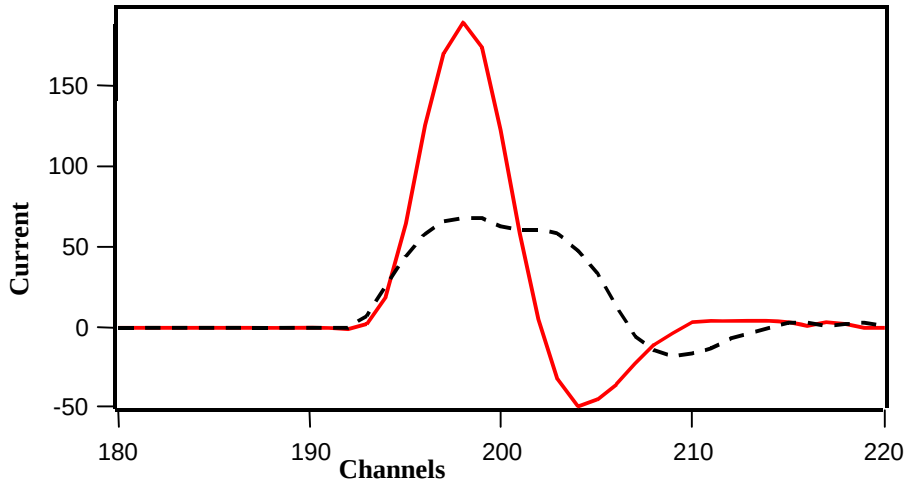

Figure 5.12: Sample electron (line) and gamma (dashed) current pulses from experiment.

Chapter 6

Timing algorithms

The key information about the pulse generated by the detection system is its time of arrival and the amplitude, corresponding to detected particle energy, of the pulse shape. These variables have to be extracted from the pulse shape very precisely. Modern day digital data acquisition systems have built-in pulse processing units that can analyze pulse shapes in real time for the time of arrival and energy with very good resolution. Traditional systems use "analog" based filtering circuitry in order to obtain this information. A Purely digital approach, which utilizes digital filters, has been possible to implement only recently, as fast real time processing units, like Digital Signal Processors or Field Programmable Gate Arrays have become available. As a result, computational filtering can now be performed in "real time". For example, results of the computation can influence whether the pulse information will be stored or rejected, or used to store or reject other information obtained simultaneously.

Simple real-time algorithms to exactly find the height, energy, of the pulse can be implemented in the digital processing units of the acquisition systems. One of them is the trapezoidal filter [XIA04, Sku99]. A good energy resolution can be achieved by choosing appropriate parameters of this filtering process. The accuracy of the determination of the pulse's arrival time for this algorithm is limited by the time stamping frequency of the digital system. A more complicated algorithm can be applied to determine the time of arrival with improved resolution, as discussed in a recent

publication [Bar04], based on stored pulse shape data. In this way a timing resolution being a fraction of the sampling frequency can be obtained. We will demonstrate it based on the 40 MSPS system, to show that a nanosecond range time resolution can be obtained even with the 25 ns sampling period.

Electronic chain

The electronic chain of the DGF acquisition system is shown in figure 6.1. The role of the pre-amplifier and signal conditioning is to bring the detector signal into the range of the ADC, which is 0-1V. The ADC is a waveform digitizer sampling at 40 MHz clock frequency, which means it samples the input signal at every 25ns. RTPU and DSP stages apply digital filters to signal, reconstruct true pulse heights and prepare data for the output. The DSP controls the whole operation of the on-board data acquisition system.

6.1 Pulse height measurement

The pulse height, which is a measure of energy, can be measured using a trapezoidal filter with appropriate peak and gap times [XIA04, Sku99]. A typical pulse shape is as shown in figure 6.2. Figure 6.3 shows the pulse shape corrected for baseline. Figure 6.4 shows the resulting pulse shape after the filtering action. The energy spectrum of ^{207}Bi decay obtained by measuring the energy using a trapezoidal filter is shown in figure 6.5. Also illustrated on figures 6.3 and 6.4 are the trapezoidal filter parameters (filter length, L, and gap time, G) and height of the pulse ($V_{x,k}$).

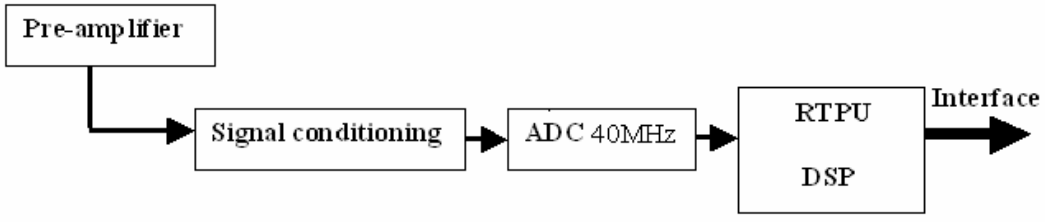

Figure 6.1: Simple electronic chain of a typical data acquisition system.

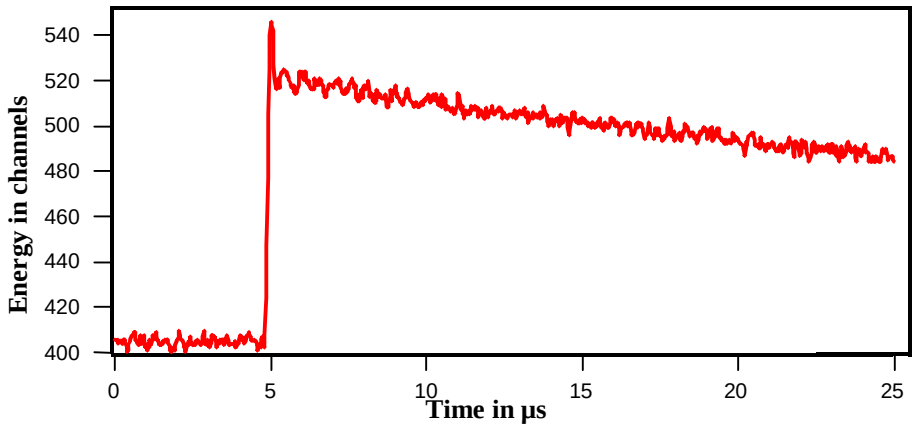

Figure 6.2: Typical Pulse shape from the detection system.

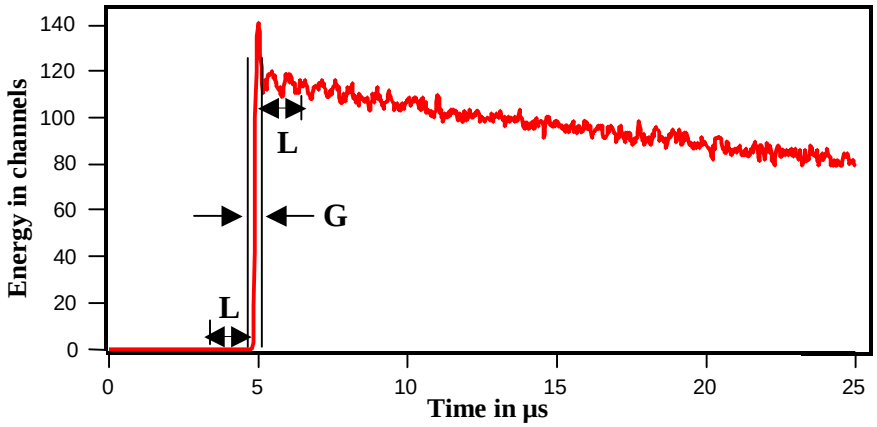

Figure 6.3: Pulse shape corrected for offset.

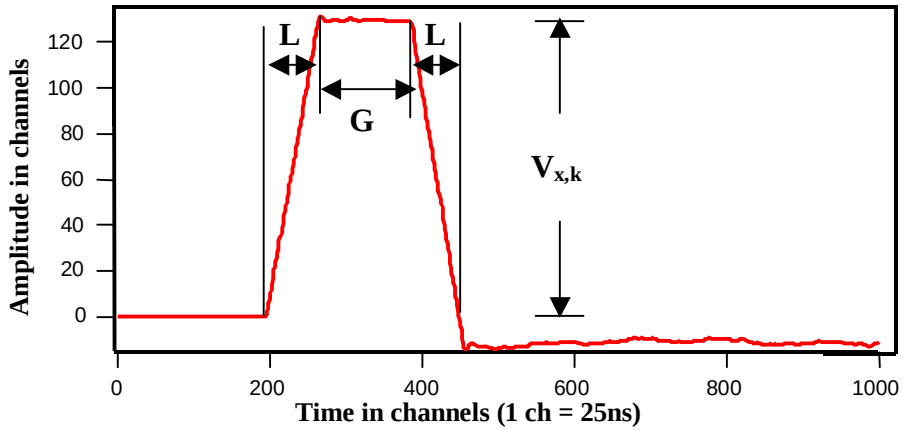

Figure 6.4: Resulting pulse shape after the filtering action.

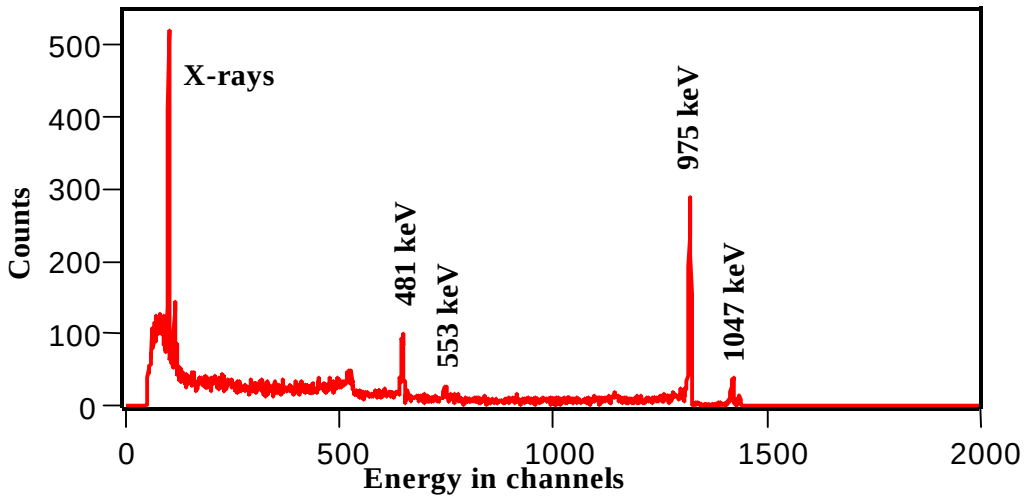

Figure 6.5: ^{207}Bi *energy spectrum as a result of digital energy filter.*

To find out the height of the pulse [XIA04], we have to average over the points before the step and subtract it from the value of the average over the points after the step.

$$V_{x,k} = -\sum_{i(before)} W_i V_i + \sum_{i(after)} W_i V_i \ .$$

Here $V_{x,k}$ is the height of the pulse and $\{W_i\}$ are the weighting values. For triangular (if the gap-time is zero) or trapezoidal the weighting values are constant. To achieve very high-speed operation the DGF4C implements the filter with fixed filter length (L) and all W_i values are equal to unity. Thus the equation implemented is:

$$LV_{x,k} = -\sum_{i=k-2L-G+1}^{k-L-G} V_i + \sum_{i=k-L+1}^{k} V_i$$

where L is the filter length (peak time) and G is the gap time. To accommodate the normalization of the weights $V_{x,k}$ is multiplied by the factor L. The pulse height (energy) can be obtained by sampling the top of the pulse shape, figure 6.4.

6.2 Timing algorithm

A similar algorithm discussed in [Bar04] is used to find the time of arrival. The time of arrival is the time when the pulse shape reaches a desired threshold. The threshold is chosen here to be 10 % of the pulse height. Ideally, the time of arrival should be the time when the pulse just starts, that is at 0% threshold, but because of the electronic noise, we have to use information about the pulse above the noise level. First an estimate of the time of arrival, t_{lin}, is found using a simple linear interpolation. Using this estimate an exact value of the time of arrival, t_{nlin}, is found. The sampling frequency of the ADC is 40MHz, which means two adjacent samples of the pulse are separated by 25ns.

Below is the detailed description of the timing algorithm.

- The pulse shape is corrected for offset, by fitting a flat straight line to the bottom of the pulse shape and subtracting it from the original pulse shape.
- The height, A (energy), of the pulse is found using an averaging filter over the flat top of the pulse, that is over the samples for which T □ t_r where t_r is the rise time of the pulse.
- Set the threshold fraction, f, at which the time of arrival will be taken.
- Threshold energy $f * A$ is found, where A is the height of the pulse.
- Two adjacent samples with amplitudes α_1 and α_2 such that $\alpha_1 < f * A < \alpha_2$ are found. See figure 6.6.
- Using linear interpolation between (α_1, t_1) and (α_2, t_2), the point $(f * A, t_{lin})$ is found. Here t_1 and t_2 are positions at which the pulse amplitude is α_1 and α_2 respectively. Also here $t_2 = t_1 + 25ns$.
- Four adjacent samples $(\alpha_0, t_0), (\alpha_1, t_1), (\alpha_2, t_2)$ and (α_3, t_3) are found. See figure6.6. Here $\alpha_0 < \alpha_1 < f * A < \alpha_2 < \alpha_3$ and $t_3 = t_2 + 25ns = t_1 + 50ns = t_0 + 75ns$.
- These four samples are interpolated using cubic spline interpolation to get a third order polynomial $f(t - t_2)$.

- The time t_{nlin} is obtained by solving the equation $f\left(t-t_2\right)=f*A$. This is achieved numerically using Newton's successive approximation method with t_{lin} as the initial guess.

Figure 6.6 shows the schematic illustration of the above-mentioned algorithm. To test this algorithm coincidence data from ^{207}Bi, as explained on page 5,taken with the Besca detection system has been used. The experimental setup used is shown in figure 3.5.

The energy spectra and the time of arrival spectra, called timing spectra from here on, for each detector have been generated. The spectrum of the time difference between the signals from each detector can then be obtained. The FWHM (Full Width at Half Maximum) of this peak will be the timing resolution. In both detectors 481 keV and 975 keV electron lines characteristic to the ^{207}Bi decay, low energy X-rays and γ-ray background have been measured, see figure 6.5. A good measure of the timing resolution will be to require the condition on the presence of the low-energy (481 keV) or high-energy (975 keV) peaks of the energy spectrum and then to look at the time difference spectrum for these events.

The timing resolution, integrated over full energy range, achieved using the above-mentioned algorithm is **9.3 ± 0.13ns**, see figure 6.8. Here *x0* is the peak position of the gaussian fit and *width* is the full width at half maximum (FWHM) of the gaussian fit. In figure 6.8 an additional 100ns is added to the timing difference in the timing algorithm to take care of the negative values. Therefore the true timing difference peak is at **10.8±0.09ns**. For Besca0 (detector 1) the timing resolution achieved is about **7.4ns** for high-energy electrons (975 keV), figure 6.14, and about **5.3ns** for low-energy electrons (481 keV), figure 6.13. For Besca1 (detector 2) the timing resolution is **13.7ns** at 975 keV and **5.9ns** at 481 keV.

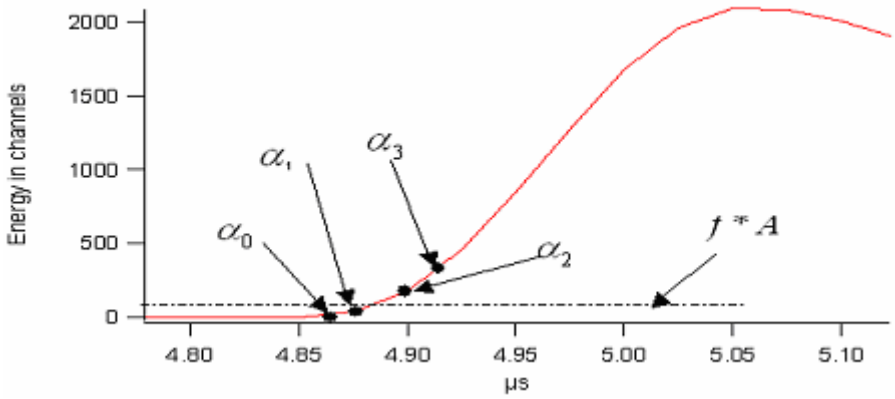

Figure 6.6: Schematic representation of the timing algorithm.

A more accurate measure of timing resolution is to choose high-energy signals from the detector, to eliminate the impact of low amplitude signals. With the ^{207}Bi source we have the monoenergetic conversion electron transitions generating strong lines at 975 keV and 481 keV, which are in coincidence and can be used to provide a timing resolution analysis. In this process we have:

I) Selected high-energy (975 keV) electrons detected in Besca0 and then generated the time difference spectrum for these events and this time only at the events near the 481 keV peak of the Besca1. This is illustrated in figure 6.7.

II) Selected lower-energy (481 keV) peak of Besca0 energy spectrum and generated the time difference spectrum for these events and this time only at the events near the 975 keV peak of Besca1. This is illustrated in figure 6.7.

The timing resolutions are **2.88ns** (gating on 975 keV line of Besca0 energy spectrum and on 481 keV line of Besca1 energy spectrum), figure 6.9, and **2.38ns** (gating on 481 keV line of Besca0 energy spectrum and 975 keV line of Besca1 energy spectrum), figure 6.10. The spectrum of energy vs. timing difference is shown in figure 6.11. We can see here that the spectrum has wide distribution at low energies and the resolution getting better at high energies. Figures 6.12 to 6.14 show the projection of 6.11 onto the bottom (time difference) axis for different energy gates (0-81 keV, 481 keV and 975 keV). Figure 6.15 shows the timing resolution at different energies.

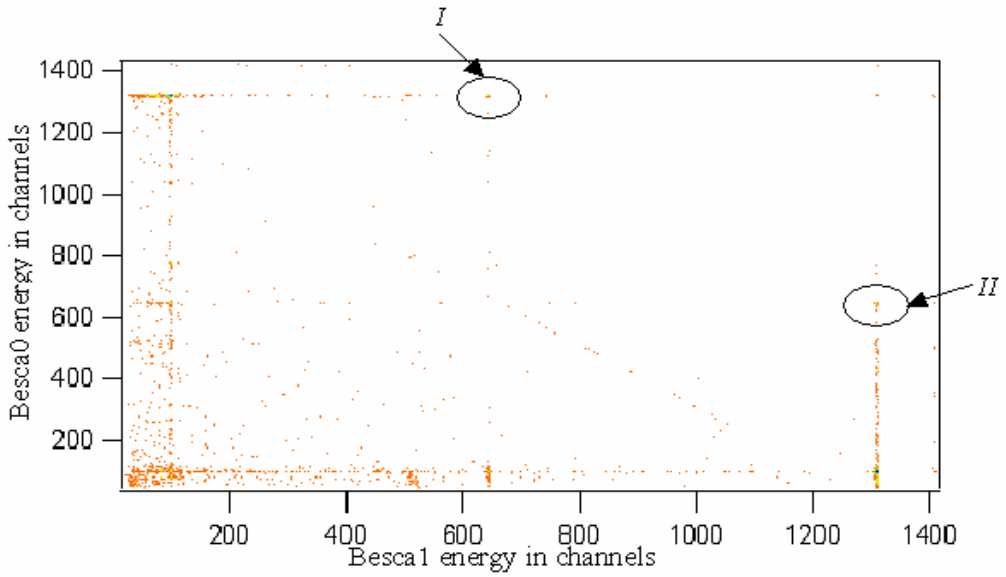

Figure 6.7: Besca1 energy vs. Besca0 energy.

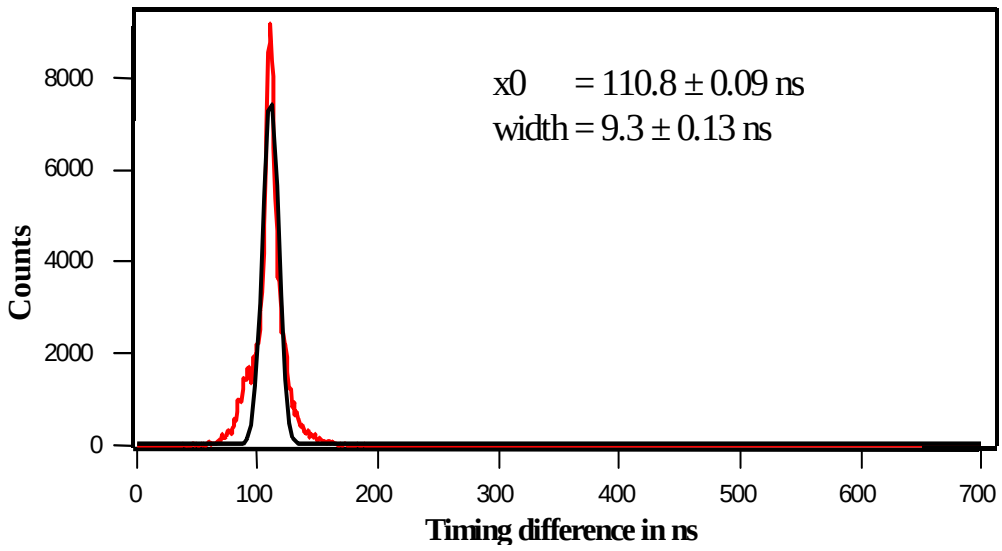

Figure 6.8: Timing resolution integrated over all energies.

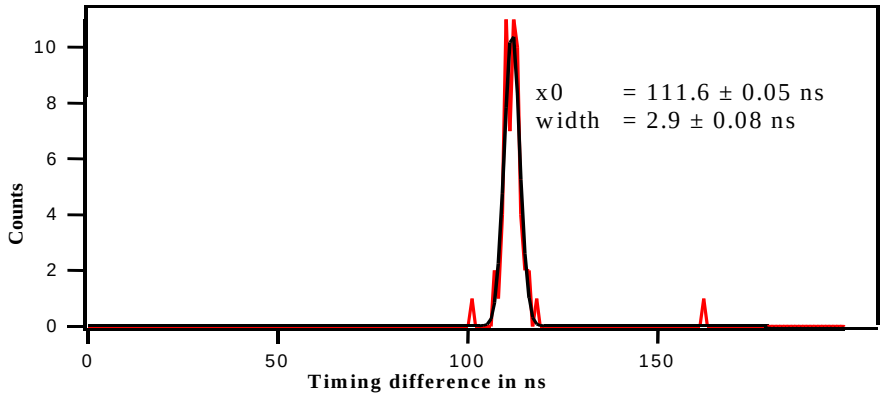

Figure 6.9: Timing resolution I).

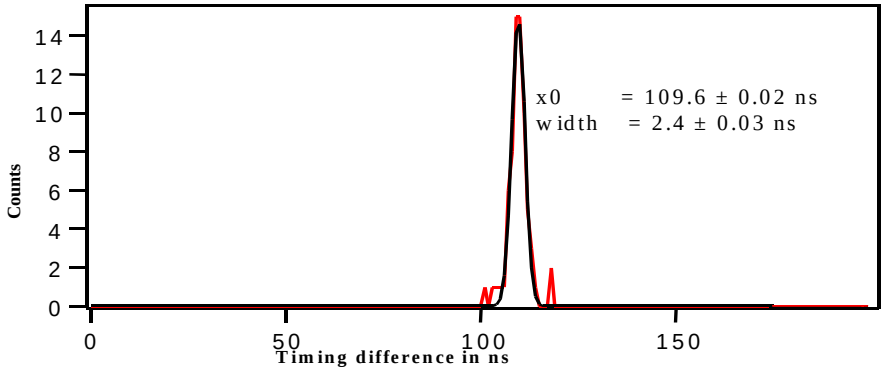

Figure 6.10: Timing resolution II).

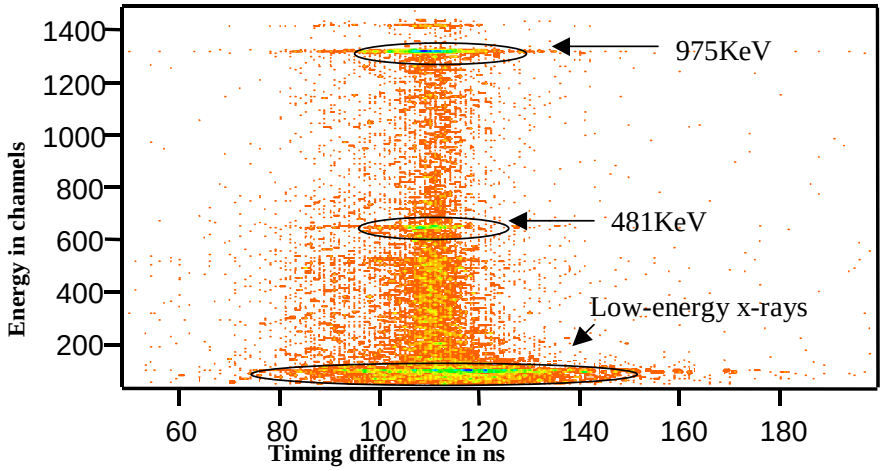

Figure 6.11: Energy vs. Timing resolution.

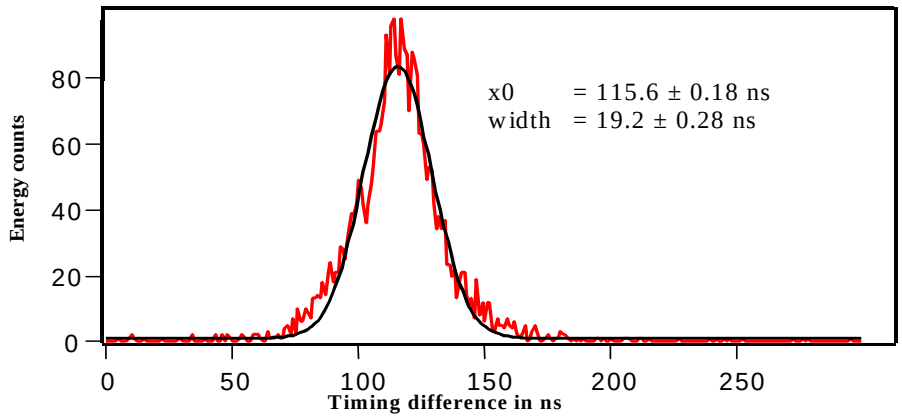

Figure 6.12: Timing difference spectrum for 0-81 keV events.

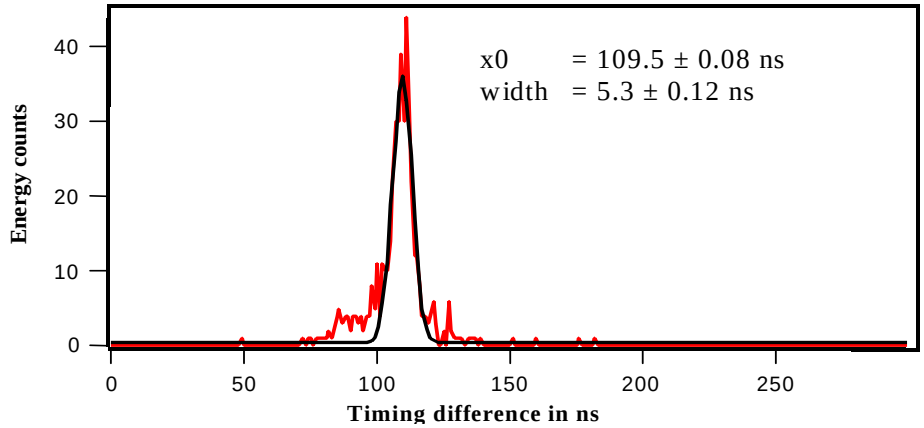

Figure 6.13: Timing difference spectrum for 481 keV events.

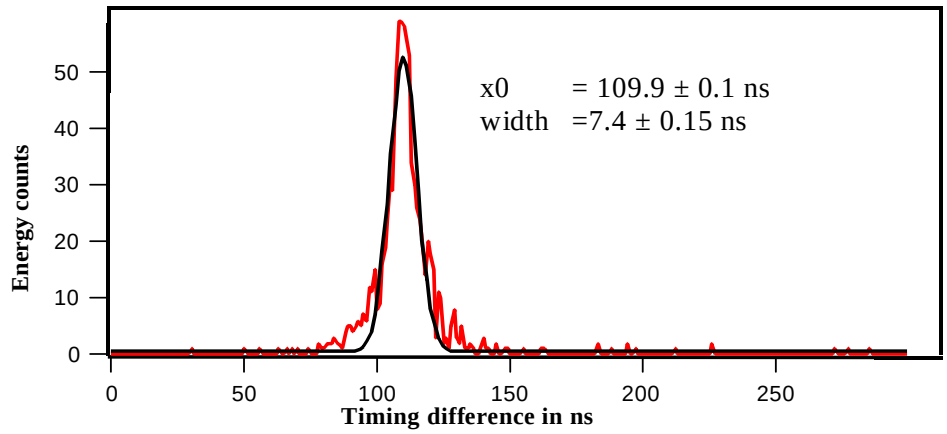

Figure 6.14: Timing difference spectrum for 975 keV events.

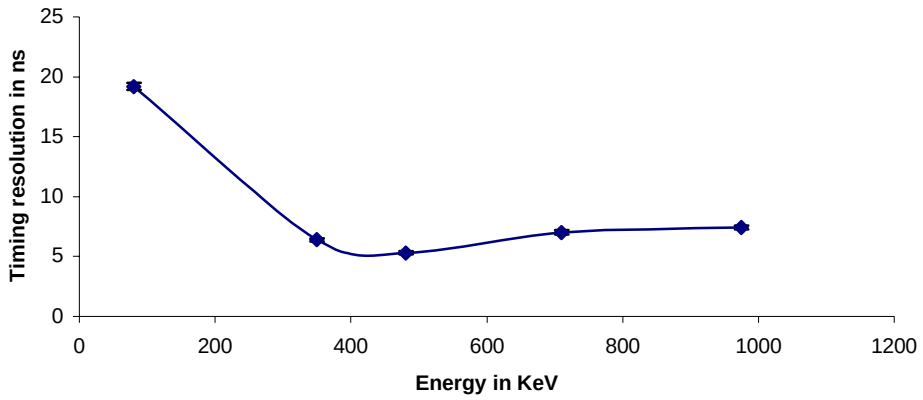

Figure 6.15: Timing resolution at different energies.

6.3 Conclusions

The above-mentioned algorithm achieves timing resolutions as good as 3ns with a 40 MSPS system. The resolution can be improved with the application of a 100 MSPS system. With a 100 MSPS system, the pulse shape has more points on the rising edge of the system. As we can see from figures 6.11 and 6.15, at low energies the timing resolution is decreasing. This can be attributed to the electronic noise in the detection system.

Chapter 7

Pulse shape analysis

As discussed in previous chapters, a study of the interaction mechanisms of radiation with matter and simulations of the pulse generation process reveals that effective discrimination between electrons and γ radiation is possible. The difference in the rise times of different pulse shapes is exploited to discriminate between electrons and gamma radiation. Since electrons interact continuously and γ radiation interacts spontaneously with the detector medium the difference in the widths of the current signals would be a good variable to distinguish electrons and γ radiation. In this chapter two algorithms developed for pulse shape discrimination between electrons and γ radiation are presented along with the statistics relating to their efficiency.

Figures 7.1 and 7.2 show a sample voltage signal from experiment and its time derivative (current signal). The valley at the end of the current pulse is caused by the oscillating part near the peak of the voltage pulse shape. This might be introduced by the oscillating circuitry in a pre-amplifier. The width of the current pulse varies with the rise time of the voltage pulse. A gaussian shape is fit to the current pulse and its Full Width at Half Maximum (FWHM) is found. Figure 7.3 shows a spectrum of FWHMs of current signals. The spectrum has a small peak to the left of the large one. From figure 5.7, we can see that current pulses generated by γ-rays have small FWHM compared to that of current pulses generated by electrons. This is a hint for a possibility of particle discrimination using pulse shape analysis.

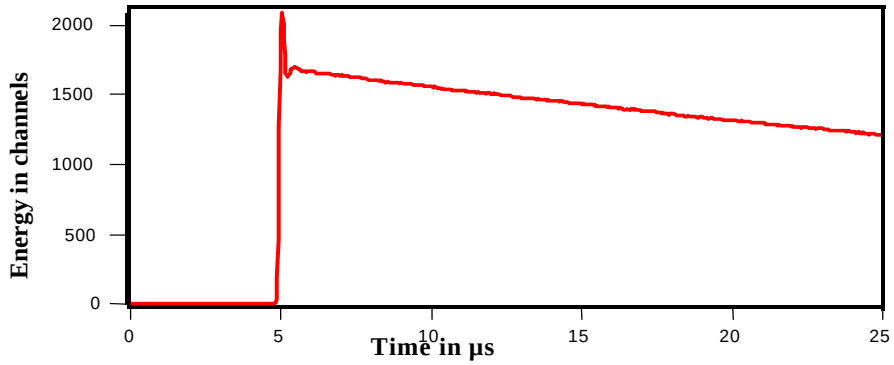

Figure 7.1: A sample Voltage Signal.

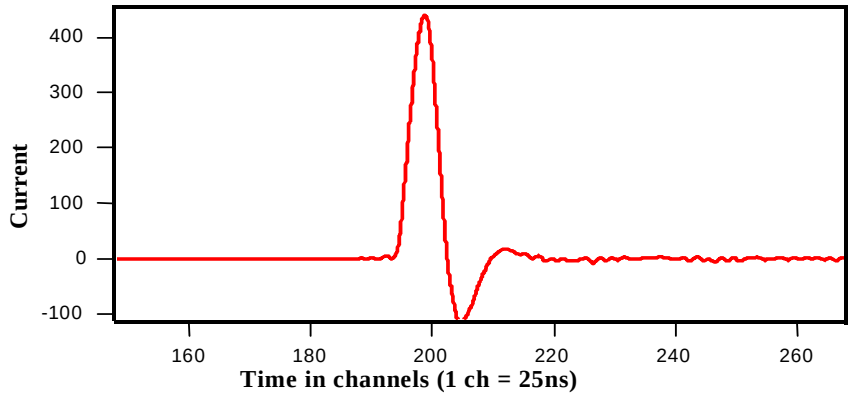

Figure 7.2: A sample Current Signal.

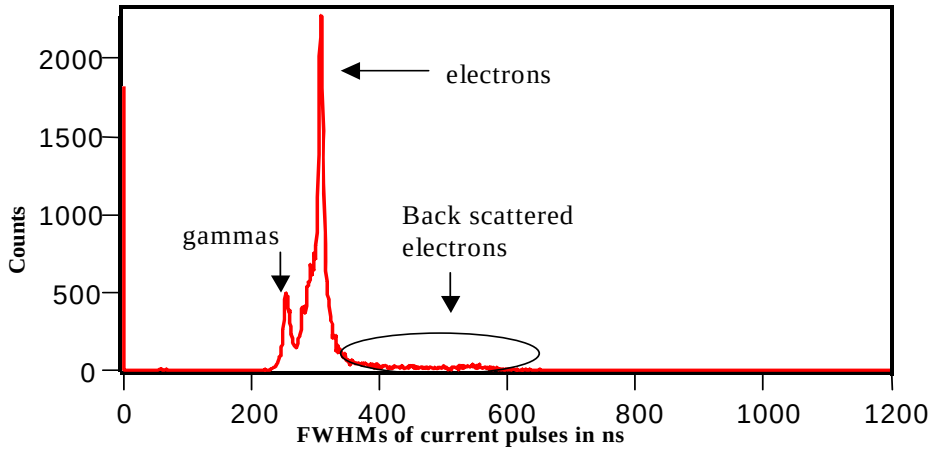

Figure 7.3: Spectrum of FWHMs of current pulses.

7.1 Algorithm 1

The changes in the shape of the current pulse, figure 7.2, near its peak calls for a variable that is independent of these shape changes. A good variable would be the difference between the peak point and the beginning point (time of arrival), which is essentially the rise time of the current pulse. In this algorithm this variable is defined and found for all pulse shapes. A plot of this variable versus the FWHM of the current pulse gives a good discrimination. The algorithm is explained below.

- The current signal, which is a time derivative of the voltage signal, is obtained for each event.
- The FWHM and the peak point of this current signal are found by fitting a gaussian.
- The time of arrival using the timing algorithm, described chapter 6, is found.
- A variable, diff_variable, is defined as the difference between the peak point and the beginning point (time of arrival) of the current pulse.
- A two dimensional histogram of the FWHM of the current signal and diff_variable is plotted.

Figures 7.4 to 7.6 show the plot of FWHMs of current pulses and diff_variable at different energy gates (81-330 keV, 330-440 keV, 481 keV and 975 keV). Figures 7.4 and 7.5 show the separation achieved by the algorithm. By analyzing figures 7.4 to 7.7, we find that the small group to the left of the large one in figures 7.4 and 7.5 can be attributed to the current signals generated by γ-rays. The large group in figures 7.4 and 7.5 can be attributed to the current pulses generated by fast electrons. However this algorithm does not give any information on other events outside these two groups in figures 7.4 and 7.5.

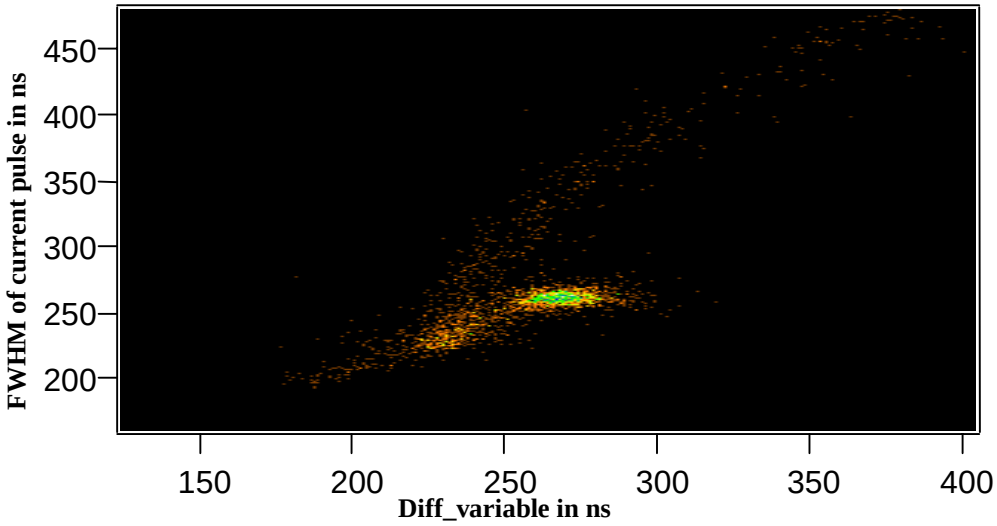

Figure 7.4: A plot of widths of current pulses versus diff_variable for a cut between 110-450 channels (81 keV-330 keV) of the energy spectrum.

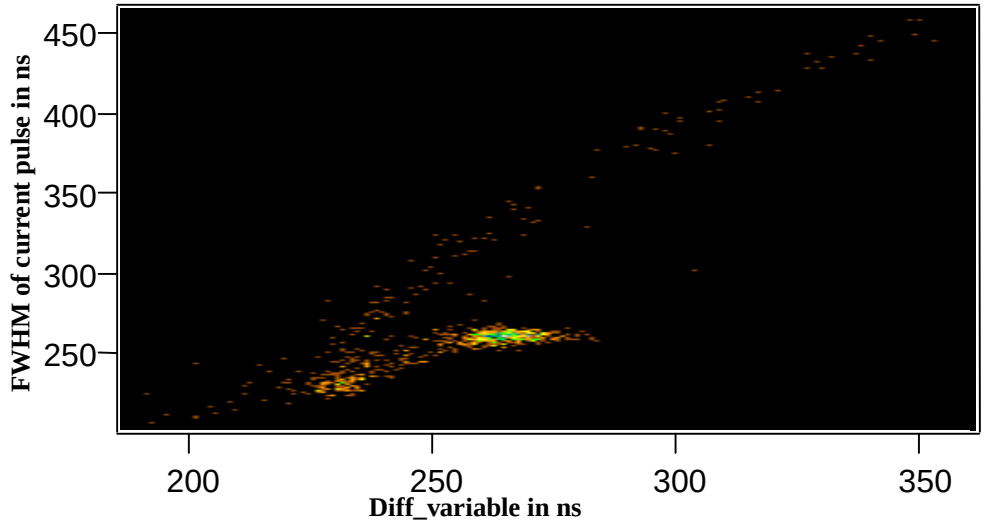

Figure 7.5: A plot of widths of current pulses versus diff_variable for a cut between 450-600 channels (330 keV-440 keV) of the energy spectrum.

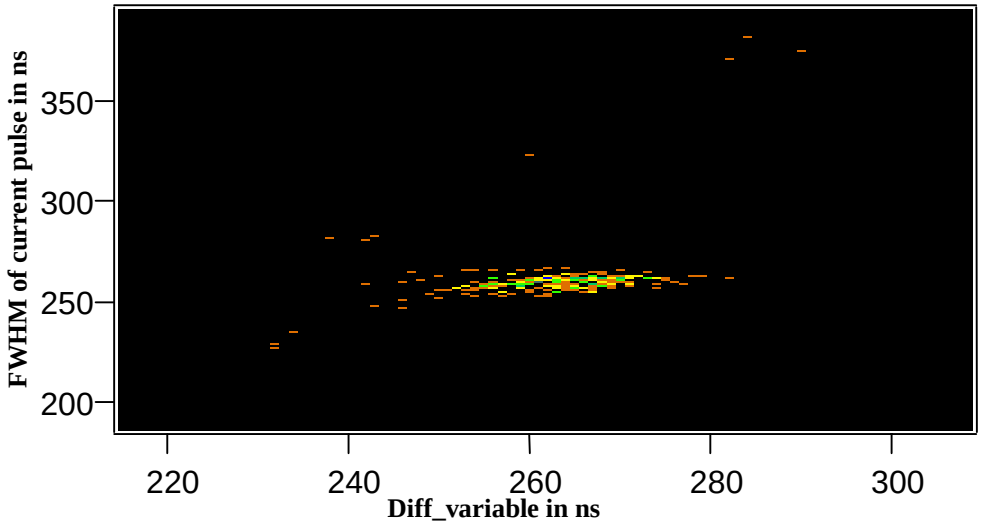

Figure 7.6: A plot of widths of current pulses versus diff_variable for 481 keV line of the energy spectrum.

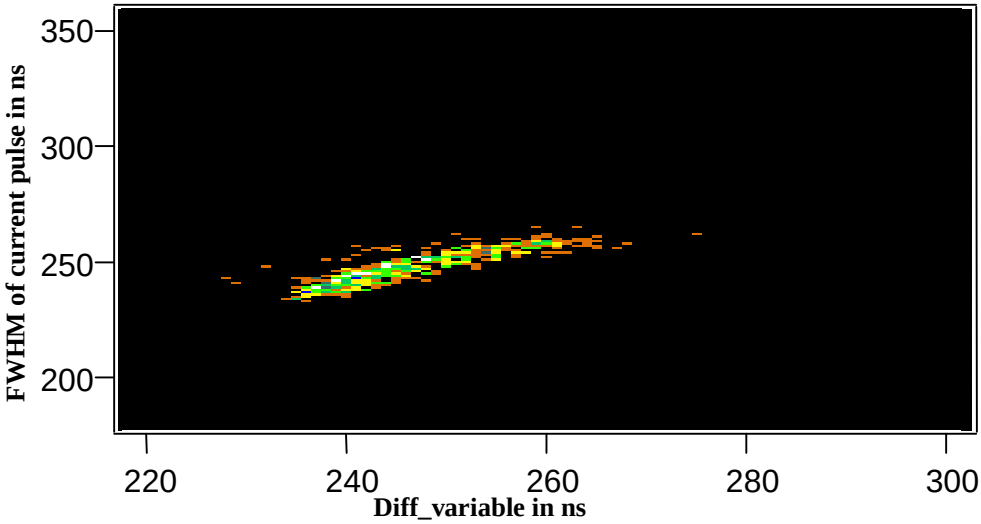

Figure 7.7: A plot of widths of current pulses versus diff_variable for 975 keV line of the energy spectrum.

Even though this algorithm achieves some separation, it suffers from poor resolution and doesn't give any useful information on discrimination and back scattered electrons. Therefore we switch to the second algorithm.

7.2 Algorithm 2

As explained previously, pulse shapes are simulated for particles interacting continuously (e^-s) and spontaneously (γs) with the detector medium at different depths. Looking at these pulse shapes, we find that at greater depths of the detector medium, current pulses generated by γ radiation have a small peak on their tails where as current pulses from fast electrons do not have these peaks, see figure 7.8. This variation can be exploited to discriminate between e^-s and γs. However at smaller depths of the detector medium, near the surface or on the surface, pulse shapes generated by either e^-s or γs do not have this peak. Therefore for these events a different variable has to be used for discrimination. By analyzing the widths of these events it is found that fitting a half-gaussian function from the peak point to the bottom point and plotting the width distribution of this fit would give a good parameter to discriminate between e^-s and γs.

The algorithm is explained as follows.

- Generate a current pulse from the voltage pulse by time differentiation.
- Smoothen the current pulse using cubic spline interpolation.
- Define a threshold level.
- Find the width (time above threshold) of the current pulse, ignoring the dips (valley at the end of the current pulse, see figure 7.2), at this threshold.
- Plot energy versus width at this threshold.
- Draw the cut-off lines for the peak of the distribution, see figure 7.11.
- For events inside these cut-off lines, fit a half-gaussian to the current pulse.
- Find σ (width of the half-gaussian fit) for this fit and plot the distribution of σ for these events.
- Draw the cut-off lines that include the electron lines and eliminate other events. This can be achieved by an energy dependent selection (gating), see figure 7.12.

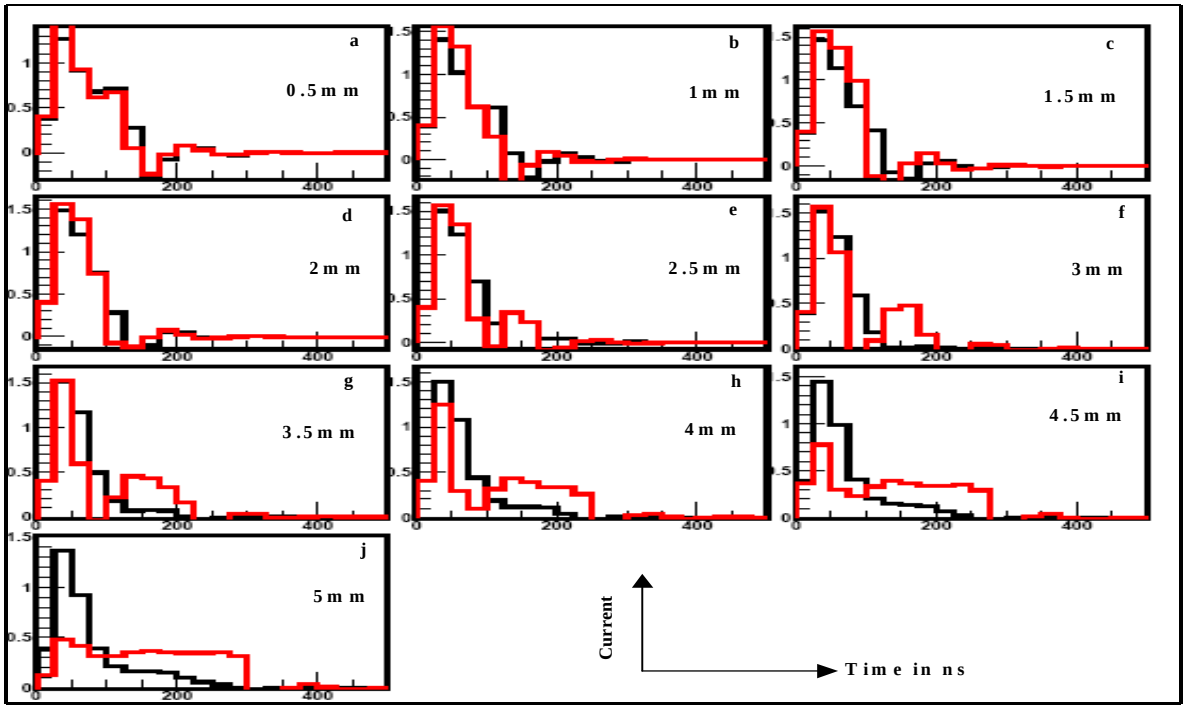

Figure 7.8: Simulated pulse shapes for both e^-s (continuous interaction, Black) and γs (point-like interaction, Red) at different depths of the detector medium.

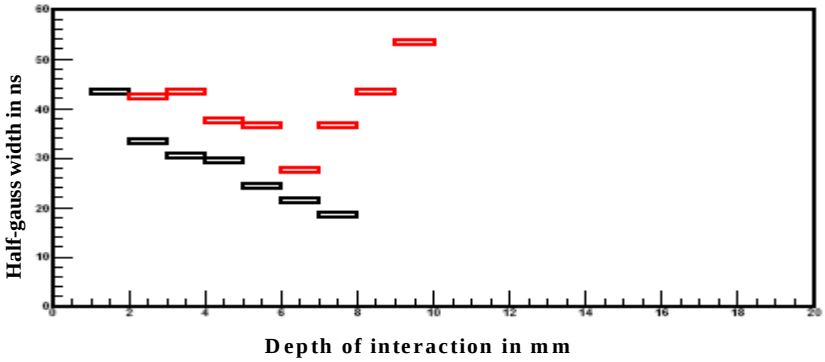

Figure 7.9: Half-gauss widths of simulated pulse shapes for both electrons (red) and gammas (black) at different depths of the detector medium.

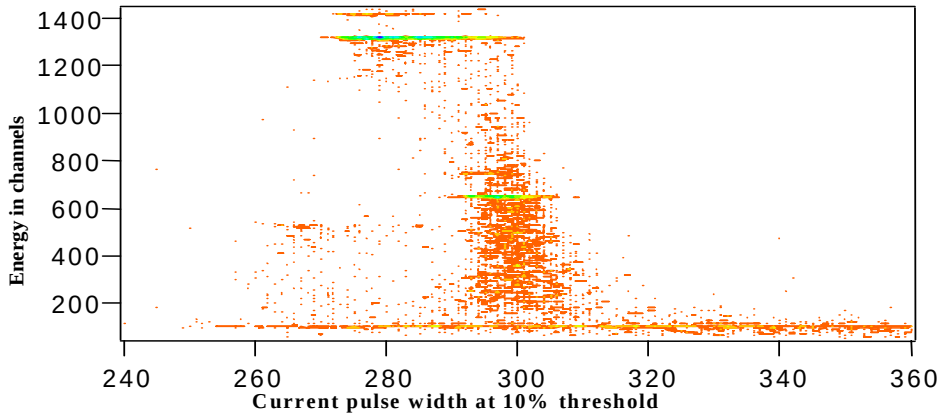

Figure 7.10: 2D plot of energy vs. width of the current pulse at 10% threshold.

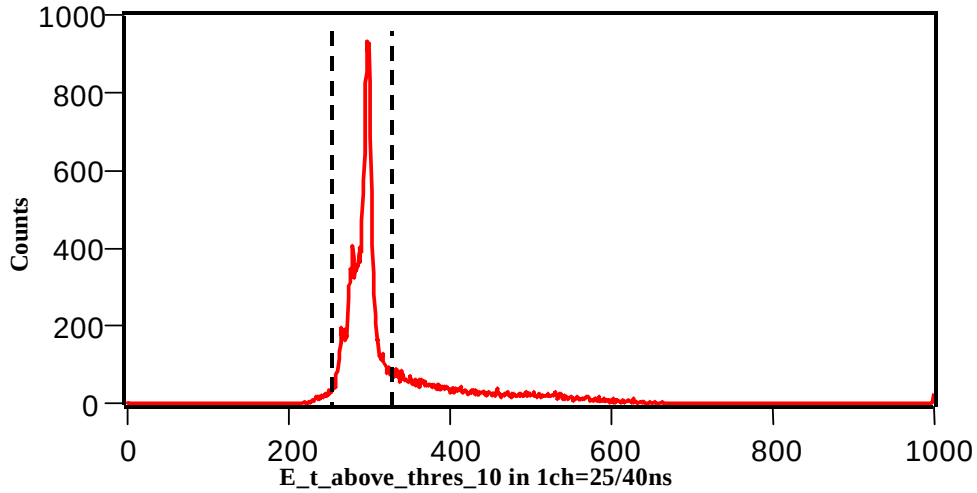

Figure 7.11: Distribution of width of the current pulse at 10% threshold.

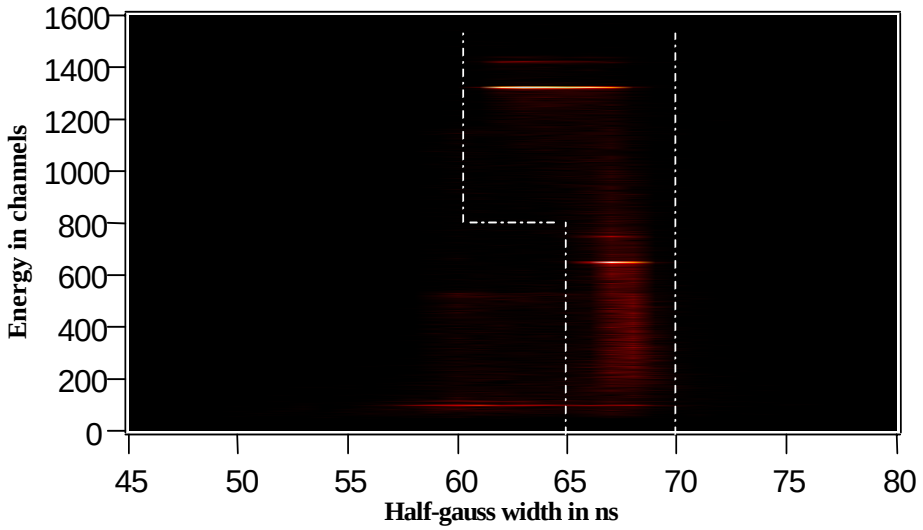

Figure 7.12: 2D plot of energy vs. width of the half-gauss fit.

Smoothening the current pulse would eliminate any glitches in the pulse, caused by the electronic noise of the detection system, which would cause uneven curve fitting. To exploit the double peaking of the current pulse caused by γ radiation at greater depths of the detector medium, a threshold level, which is as small as possible, is defined. A large threshold level might overlook the double peaking and might not give a good discrimination. For this algorithm 10% of the peak values is found to be the optimum threshold level. Figure 7.10 shows the plot of energy against the width of the current pulse at 10% threshold. We can clearly see the groupings at 481 keV and 975 keV electron lines. Figure 7.11 shows the distribution of the widths of current pulses at 10% threshold. This indicates that current pulse width is a good parameter to start discriminating with. With this parameter we can distinguish between electrons and γs from e-j in figure 7.8.

As we can see from figure 7.11 there are still a lot of events remaining in or near the peak. From figure 7.8 we can see that electron and gamma radiation interacting on or near the surface of the detector have very little distinguishable difference in their widths at 10% threshold (a-d in figure 7.8). Figure 7.9 shows the plot of fall time of the current pulses simulated for both electrons and γ-rays at different depths of interaction in the

detector medium. We can see that at smaller depths current pulses generated by electrons have slower fall times compared to the fall times of the current pulses by γ-rays. To further discriminate among events that are in or near the peak in figure 7.11 the differences in fall times of the current pulses are exploited. For these pulses the peak and bottom points are identified. A half-gaussian shape is fitted from the peak to the bottom point of the current pulse. The width of this fit, which describes the fall time of the current pulse, is found and can be used to further discriminate between electron and gamma radiation. Figure 7.12 shows the plot of energy against the fall time of the current pulse.Figure 7.13 shows the distribution of half-gaussian widths of the current pulses, for events on the peak in figure 7.11. Figures 7.14 and 7.15 show the distribution of half-gaussian widths for 481 keV and 975 keV events. Figure 7.16 shows the energy spectrum before applying the algorithm, referred to as "original" spectrum. Figure 7.17 shows the final energy spectrum after applying the algorithm, referred to as the "cleaned" spectrum. Looking at these two spectra we can see that the algorithm has significantly reduced the γ ray background mostly at low-energies. Figure 7.18 shows "original" and "cleaned" spectra plotted together.

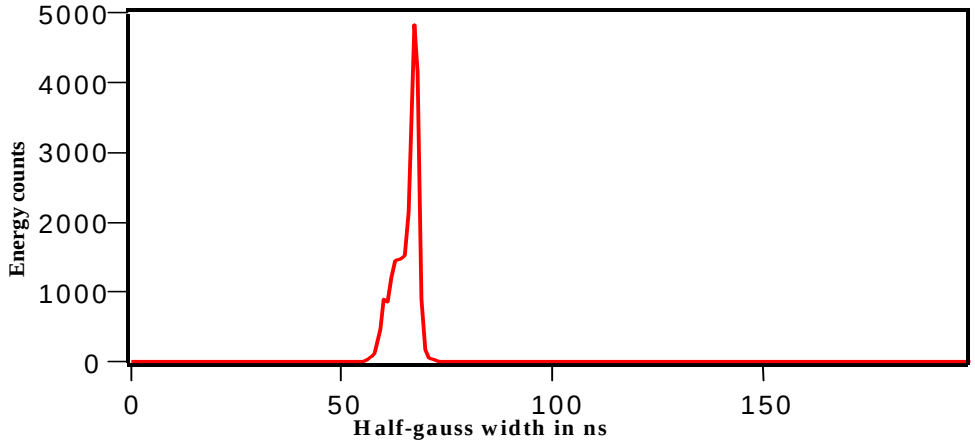

Figure 7.13: Distribution of half-gauss widths for all events.

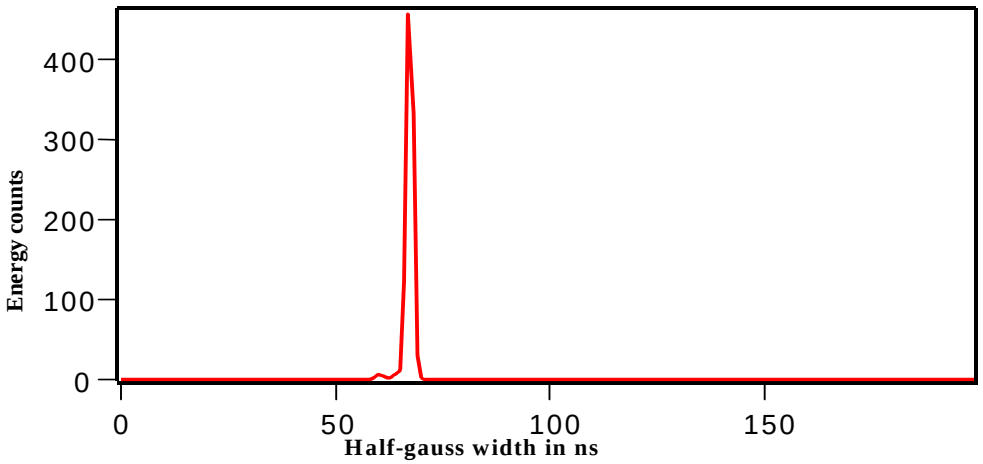

Figure 7.14: Distribution of half-gauss widths for events on 481 keV electron line.

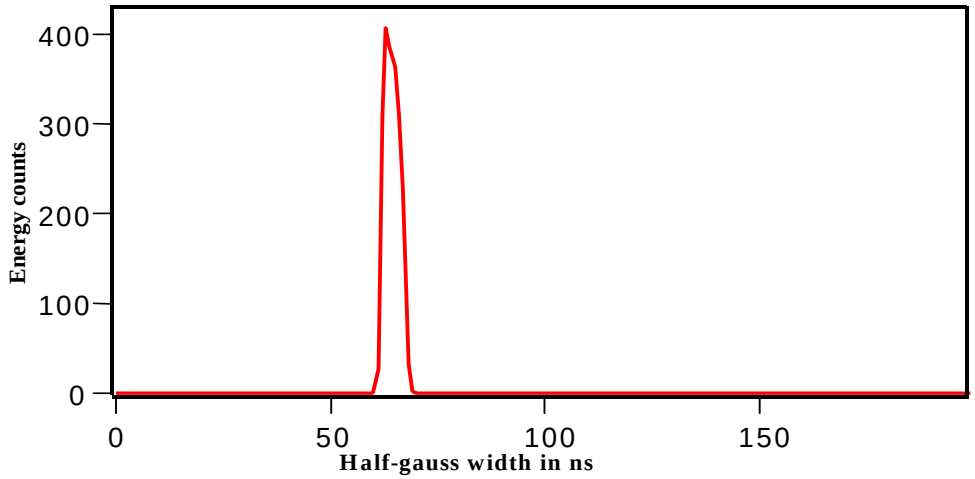

Figure 7.15: Distribution of half-gauss widths for events on 975 keV electron line.

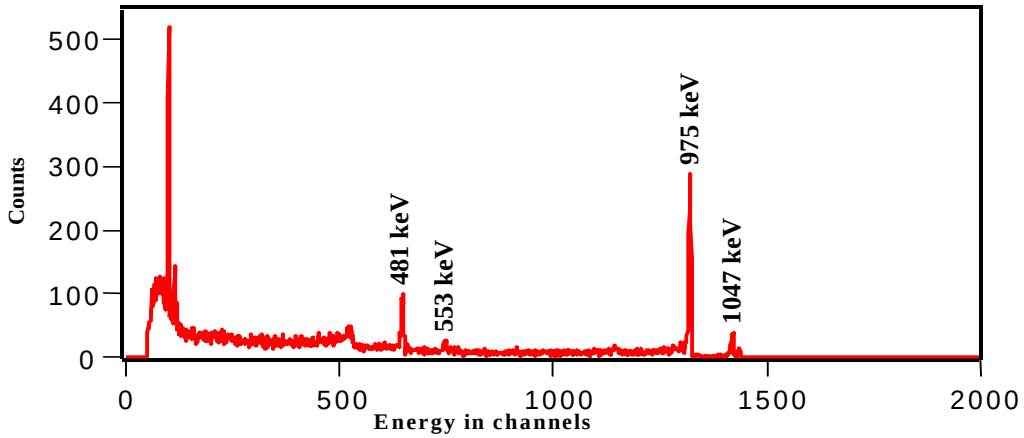

Figure 7.16: Energy spectrum before the algorithm.

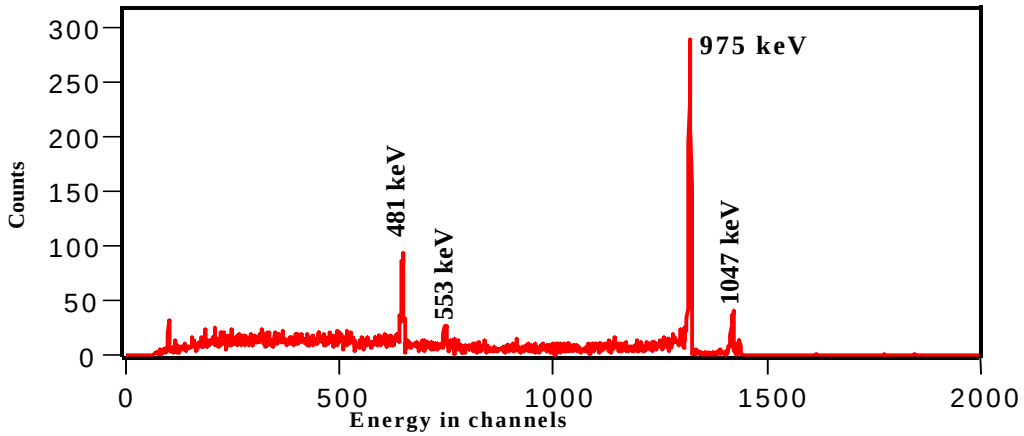

Figure 7.17: Energy spectrum after applying the algorithm.

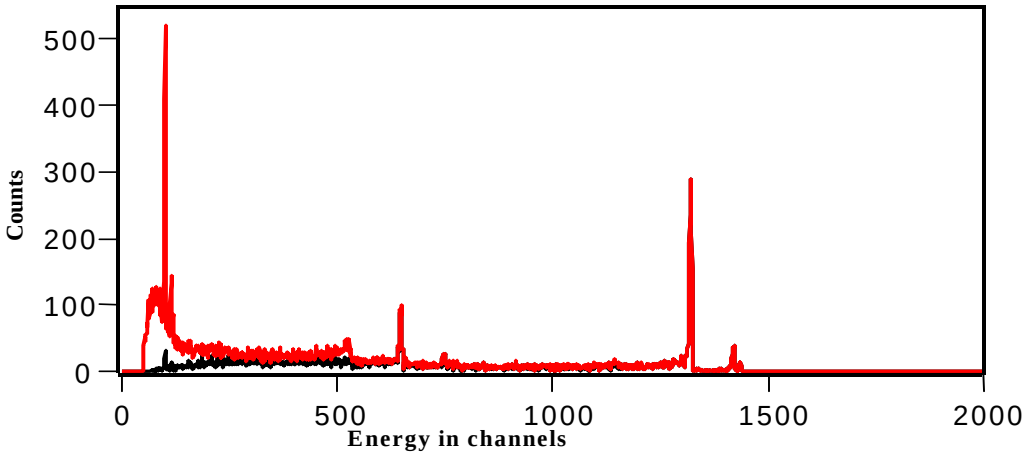

Figure: 7.18: Overlapping of "original"(red) and "cleaned"(black) spectra.

Efficiency of the algorithm

The efficiency of the algorithm in discriminating between electrons and gamma radiation can be calculated as follows.

The original spectrum has a total of 31090 events. The cleaned spectrum, the spectrum after the algorithm, has a total of 15690 events. Therefore the total number of events rejected by the algorithm is $31090 - 15690 = 15400$, 11509 counts were removed in the first step of the algorithm (current pulse width at 10% threshold) and 4605 in the second step of the algorithm (half-gauss fit to the current pulse).

The original spectrum has a total of 1031 events in the 481 keV electron line and the cleaned spectrum has a total of 962 events in the 481 keV electron line. The total number of events in the 975 keV electron line in the original spectrum is 2069 and in the cleaned spectrum the 975 keV line has 2062 events. The original spectrum has a total of 266 events in the 533 keV electron line and the cleaned spectrum has a total of 246 events in the 533 keV electron line. The total number of events in the 1047 keV electron line in the original spectrum is 306 and in the cleaned spectrum the 1047 keV line has 305 events. We can see that the algorithm has rejected

$(1031 - 962) + (2069 - 2062) + (266 - 246) + (306 - 305) = 97$ electron events.

The original spectrum has a total of 7274 low energy x-rays (0-81 keV). The cleaned spectrum has a total of 248 low energy x-rays. Therefore the total number of low energy x-rays rejected by the algorithm is $7274 - 248 = 7026$. This leaves a total of $(15400 - 7026) = 8374$ events rejected by the algorithm which are not low energy x-rays. Since the electron lines are well preserved by the algorithm, except for 97 events, we can say that the total number of γ events rejected by the algorithm is $(8374 - 97) = 8277$.

To find the efficiency of the algorithm we need to find the total number of γ events present in the original spectrum. Figure 7.19 shows the decay data set of ${}^{207}_{83}Bi \rightarrow {}^{207}_{82}Pb$ [NNDC].

The total number of 481 keV electrons in the original spectrum is 1031. From the branching ratios we can find that there would have been

$\frac{97.76}{1.515} * 1031 = 66,528$ of 570 keV γ ray events,

$\frac{74.6}{1.515} * 1031 = 50,767$ of 1060 keV γ ray events and

$\frac{6.87}{1.515} * 1031 = 4,675$ of 1770 keV γ ray events.

From gamma interaction probability calculations [Kan95] we can find that only 9% of 570 keV γ rays, 6.71% of 1060 keV γ rays and 5.21% of 1770 keV γ rays would interact with the detector.

Electrons		**Gamma Radiation**	
Energy	Branching Ratio	Energy	Branching Ratio
481KeV (K-shell)	1.515%	570 KeV	97.76%
553KeV (L-shell)	0.438%	1060 KeV	74.6%
975KeV (K-shell)	7.03%		
1047KeV (L-shell)	1.84%		

Figure 7.19: Decay data set of $^{207}_{83}Bi \rightarrow {}^{207}_{82}Pb$ *[NNDC].*

Therefore a total of 5987 570 keV γ rays, 3406 1060 keV γ rays and 243 1770 keV γ rays would interact with the detector. Therefore the total number of γ rays originating from ^{207}Bi in the original spectrum is 9636. The 570 keV, 1060 keV and 1770 keV peaks are not seen in the decay spectrum of 207Bi, figure 7.16, because the thickness of the Si(Li) detector of the BESCA detection system is not thick enough (5mm thick) and also, the full energy of the γ-ray is not deposited in the detector, only a fraction of the energy is transferred (by recoil) in Compton scattered events.

The efficiency of the algorithm is therefore

$$\frac{8277}{9636} = 0.8589 = 85.89\%.$$

Conclusions

The events that passed this algorithm are predominantly electrons. However, there still many events that are left over. This can partially be attributed to the fact that electrons and gamma-rays interacting on or near the surface of the detector have almost identical pulse shapes, see figure 7.8 (a,b,c). But non-suppressed gamma ray events most likely form only a small fraction of about 11% of the remaining 12115 events (not counting mono-energetic electrons). The remaining 89% are most likely true electrons from Compton scattering effect outside the Silicon material in the detector (for example on source backing or detector window), thus generating genuine electron events penetrating through the front surface of the detector. Other methods to suppress these events have to be devised.

Chapter 8

Conclusions

In this work, applications of fast digital electronics in gamma and conversion electron spectroscopy have been investigated. The advantages of digital electronics over conventional analog electronics have been discussed.

The ability to capture the detector's pulse shape has been utilized and numerical algorithms have been developed to study signals from a solid state Si(Li) detector. Using the Ramo-Shockley theorem [Ram39, Sho38, Zho01] and properties of interaction mechanisms of electrons and gamma radiations with matter [Leo94, Kno99], an algorithm to simulate the pulse shapes generated by electron and gamma radiations in planar Si(L) detector was devised. The algorithms, discussed in [Bar04], are implemented for the ^{207}Bi conversion electron data measured by the Si(Li) detector called BESCA. With this algorithm a timing resolution as good as 2.5 ns is achieved. Another algorithm to effectively discriminate between electrons and gamma radiation is developed using the pulse shape analysis. The aim was to suppress the gamma ray background in the ^{207}Bi conversion electron spectrum. The algorithm has achieved a discrimination efficiency of about 86%. There are still non-suppressed gamma ray induced events present in the spectrum. Other methods to effectively suppress these events have to be developed.

The pulse shape discrimination algorithm can be applied to situations where the gamma-ray background is significantly large and makes it very difficult to observe weak electron transitions. The timing algorithm can be applied to experiments, which require great precision in timing information.

Bibliography

Bibliography

[Amm63] C.A.J . Ammerlaan et al., Nucl. Inst. Meth. Phys. Res. 22, 189 (1963).

[App61] Appelmon, Phys. Rev. Lett. 21 (1961).

[Bar04] L. Bardelli et al., Nucl. Inst. Meth. Phys. Res. A 521, 480 (2004).

[Bat03] J.C. Batchelder, Nucl. Inst. Meth. Phys. Res. B 204, 625 (2003).

[Cav71] G. Cavalleri et al., Nucl. Inst. Meth. Phys. Res. 92 137 (1971).

[Del99] M.A. Deleplanque et al., Nucl. Inst. Meth. Phys. Res. A 430, 292(1999).

[Grz03] R. Grzywacz, Nucl. Inst. Meth. Phys. Res. B 204, 649 (2003).

[Hub99] B. Hubbard-Nelson et al., Nucl. Inst. Meth. Phys. Res. A 422, 411(1999).

[Jen41] C.K. Jen, Proceedings of the I.R.E., June 1941, p. 345.

[Kno99] Glenn F. Knoll, Radiation Detection and Measurement, John Wiley & Sons, New Jersey, (1999).

[Kar03] M. Karny et al., Phys. Rev. Lett. 90, 012502 (2003).

[Kan95] J. Kantele, Handbook of Nuclear Spectrometry, Academic Press, San Diego, 1995.

[Leo94] W.R. Leo, Techniques for Nuclear and Particle Physics Experiments, Springer-Verlag, New York, (1994).

[Lid06] S. Liddick et al., Phys. Rev. Lett. (2006).

[Mih01] L. Mihailescu, Principles and methods for gamma-ray tracking with large volume germanium detectors, Doctoral thesis, University of Bonn, 2001.

[Mut99] M. Mutterer et al., Nuclear Science Symposium, 1999. Conference Record. IEEE Volume 1, 148 – 151, 1999.

[Mom00] M.Momayezi et al., Proceedings of International Symposium on Proton-Emitting Nuclei, 1999, AIP 518 p. 307, (2000).

[NNDC] National Nuclear Data Center. (http://www.nndc.bnl.gov/)

[ORT] Modular Pulse Processing and Semiconductor Radiation Detectors, ORTEC Manual. (http://www.ortec-online.com/)

[Pau94] G. Pausch et al., Nucl. Inst. Meth. Phys. Res. A 337, 573 (1994).

[Pie00] A. Piechaczek et al., Phys. Rev. C 61, 047306 (2000).

[Pix04] XIA, Pixie16 User's Manual, 2004.

[Ram39] S. Ramo, Proceedings of the I.R.E., September 1939, p. 584.

[Sho38] W. Shockley, J. Apply. Phys. 9 (1938) 635.

[Sku99] W. Skulski et al., NATO Advanced research Workshop on Techniques and Selected Applications in Nuclear Physics, 1999.

[Tan06] M.N. Tantawy et al., Phys. Rev. C **73**, 024316 (2006)

[Vet00] K. Vetter et al., Nucl. Inst. Meth. Phys. Res. A 452, 223 (2000).

[Vet01] K. Vetter et al., Nucl. Phys. A 682, 286c (2001).

[XIA] http://www.xia.com/

[XIA04] XIA, DGF-4C Users's Manual, 2004.

[Zho01] Zhong He, Nucl. Inst. Meth. Phys. Res. A 463, 250 (2001).

Vita

Rama S Katakam was born in Kakinada, India. He graduated with a bachelors degree in Electrical Engineering from Jawaharlal Nehru Technological University (JNTU), Kakinada. He went to Wright State University, Dayton, OH for his masters degree in Electrical Engineering. He joined The University of Tennessee, Knoxville, in the fall of 2004 and started working with the UT/HRIBF Nuclear Structure group. He plans to continue with his Phd at UT.